Geochemistry Geophysics Geosystems G3
AN ELECTRONIC JOURNAL OF THE EARTH SCIENCES
Published by AGU and the Geochemical Society

Technical Brief
Volume 9, Number 3
26 March 2008
Q03022, doi:10.1029/2007GC001773
ISSN: 1525-2027

An accuracy assessment of the fan wavelet coherence method for elastic thickness estimation

J. F. Kirby and C. J. Swain

Institute for Geoscience Research, Department of Spatial Sciences, Curtin University of Technology, GPO Box U1987, Perth, Western Australia 6845, Australia (j.kirby@curtin.edu.au; c_swain@wt.com.au)

[1] A variety of methods exist to estimate the elastic thickness (T_e) of the lithosphere. In this contribution, we attempt to provide an indication of how well the fan wavelet coherence method recovers T_e, through synthetic modeling. The procedure involves simulating initial topographic and subsurface loads and emplacing them on a thin elastic plate of known T_e, generating the postloading topography and gravity. We then attempt to recover that T_e distribution from the gravity and topography through the wavelet method, hence discovering where its strengths and weaknesses lie. The T_e distributions we use here have elliptical and fractal geometries, while the initial loads are fractal. Importantly, we have found that this widely used synthetic loading calibration method will tend to result in underestimates of T_e no matter which recovery method is used. This is due to random correlations between the initial loads which, on average, serve to increase their coherence at all wavelengths and spatial locations. For the fan wavelet method, the degree of underestimation from this "background" source is approximately 10% of the true T_e. In addition, the fan wavelet coherence method will provide underestimates of (1) the true T_e when the study area size is of the order of the highest flexural wavelength or less, (2) relative T_e differences when the T_e anomaly is narrow compared to its flexural wavelength, and (3) steep T_e gradients. Significantly, we find that the recovery is not greatly affected by the assumption of uniform T_e in the inversion of the coherence. We also find that T_e recovery from the coherence is only weakly dependent upon the initial subsurface-to-surface loading ratio (f). In contrast to the coherence, T_e recovery from the admittance is highly "noisy," with discontinuities and overestimates of T_e frequently arising. This is most likely due to the high sensitivity of the admittance to f and is likely to apply to real data as well.

Components: 12,893 words, 18 figures, 1 table.

Keywords: elastic thickness; wavelets.

Index Terms: 8138 Tectonophysics: Lithospheric flexure; 8159 Tectonophysics: Rheology: crust and lithosphere (8031).

Received 31 July 2007; **Revised** 12 November 2007; **Accepted** 28 January 2008; **Published** 26 March 2008.

Kirby, J. F., and C. J. Swain (2008), An accuracy assessment of the fan wavelet coherence method for elastic thickness estimation, *Geochem. Geophys. Geosyst.*, *9*, Q03022, doi:10.1029/2007GC001773.

1. Introduction

[2] A relatively recent development in the spectral method of elastic thickness estimation saw the introduction of the continuous wavelet transform (CWT), in which the spectral properties of a signal are localized at each grid point. This feature lends itself to flexural analyses, where the flexural rigidity of the lithosphere can vary spatially. *Stark et al.* [2003] based their analysis upon the derivative of Gaussian (DOG) wavelet family, while *Kirby and*

Swain [2004] used rotated Morlet wavelets in a so-called "fan" geometry. Applications of these methods were made to southern Africa by *Stark et al.* [2003], and to the Irish Atlantic margin by *Daly et al.* [2004] using the DOG wavelets; and by *Swain and Kirby* [2006] to Australia, and *Tassara et al.* [2007] to South America using the fan wavelet.

[3] The effectiveness of any data analysis/inversion method when estimating T_e can be assessed through synthetic modeling, first developed by *Macario et al.* [1995]. In this study, we apply the (isotropic) fan wavelet coherence method to synthetic gravity and topography data generated from the flexure of a thin elastic plate with known values of both elastic thickness (T_e), and ratio between the initial subsurface and surface load amplitudes (f). In this fashion, we hope to determine a measure of this method's T_e recovery capability in a variety of simulated tectonic settings. In brief, a wavelet coherence is computed at each grid node of the data area (Appendix B), then inverted for estimates of both T_e and f (Appendix C). In the work by *Kirby and Swain* [2004] we used the expression for the theoretical coherence and an assumed, uniform value for f (i.e., constant in both space and wave number domains), which we call the "uniform f method." However, in the work by *Swain and Kirby* [2006] we extended the method of *Forsyth* [1985] to compute a predicted wavelet coherence, which provides both T_e and f estimates directly from the observed gravity and topography data: the "wavelet-Forsyth method." For completeness, in Appendix C2 we give the wavelet versions of the *Banks et al.* [2001] equations, because we used this method in the work by *Tassara et al.* [2007]. Finally, we also present a new algebraic method to estimate the coherence transition wavelength (Appendix D).

2. Synthetic Models

2.1. Model Generation

[4] Two grids, generated by a random process and having fractal spectra, are taken to be the initial surface and subsurface loads acting on a thin elastic plate of known T_e and f. We used the RAN2 random number generator from *Press et al.* [1992] and the spectral synthesis method of *Peitgen and Saupe* [1988] to generate the load surfaces, with both surfaces having fractal dimensions of 2.5, unless otherwise specified. *Macario et al.* [1995] determined that the recovered T_e is relatively insensitive to the choice of fractal dimension, a result we have also found with the wavelet method. In all synthetic models we take the subsurface loading to occur at the Moho, to which we assign a mean depth of 35 km, and, unless otherwise specified, we set $f = 1$. All grids used in the synthetic modeling were generated with a 20 km grid spacing, and, unless otherwise specified, had dimensions of 5100 × 5100 km.

[5] For nonuniform T_e distributions, the deflections of the loaded plate must be obtained by a numerical solution of a fourth-order partial differential equation (Appendix A). We employed a finite difference method of solution with periodic boundary conditions. The resulting deflections of the surface and Moho interfaces then give the final topography and Bouguer gravity anomaly of the plate.

2.2. Land/Ocean Loading

[6] Since many study areas contain both continental and oceanic lithosphere, with the latter being subject to an additional water load, we developed synthetic models that account for this, to test whether our inversion equations were valid in such "mixed-loading" regimes. Starting with the initial fractal loads, where negative values of the topography indicate oceanic regions, the final loads after flexure are determined by an iterative procedure which accounts for water infilling the depressions below "sea level" after each flexure iteration. A stable value of the final topography is usually reached after five iterations.

[7] Then, rather than performing two separate analyses and inversions on land and ocean areas, as did *Pérez-Gussinyé et al.* [2004], we scale oceanic bathymetry to an equivalent topography before wavelet transformation, as was done by *Stark et al.* [2003], and compute T_e for the whole area (in one run) using only the land-loading equations. We did this because we found that using actual bathymetry and mixed-loading inversion equations gave T_e discontinuities at the coastlines. And though we have not tried it, we suspect that the masking method of *Pérez-Gussinyé et al.* [2004] will also generate coastline discontinuities due to Fourier transform edge effects. The equivalent topography at sea is computed from actual bathymetry (h) via:

$$h(\mathbf{x}) \rightarrow \left(\frac{\rho_c - \rho_w}{\rho_c}\right) h(\mathbf{x}) \qquad \forall h(\mathbf{x}) < 0 \qquad (1)$$

and represents the location of the sea floor as what it would be if there were no water present

Table 1. Symbols and Values of Constants

Constant	Symbol	Value	Units
Young's modulus	E	100	GPa
Newtonian gravitational constant	G	6.67259 $\times 10^{-11}$	$m^3kg^{-1}s^{-2}$
Poisson's ratio	ν	0.25	
Acceleration due to gravity	g	9.79	ms^{-2}
Mean Moho depth	z_m	35	km
Mantle density	ρ_m	3300	kg m^{-3}
Crustal density	ρ_c	2800	kg m^{-3}
Sea water density	ρ_w	1030	kg m^{-3}

(provided isostasy operates). Values of the densities are given in Table 1.

[8] This method also makes an approximation in the inversion relationships in the oceans: even with equivalent topography, use of the land-loading deconvolution equations at sea biases the recovered T_e to higher values and f to lower values. While we do not correct for this bias at present, Appendix C3 shows how it can be modeled, with the bias being less than the likely T_e error. Nevertheless, the results from our synthetic modeling do show a slight upward bias when we invert for T_e from mixed-loading models, and are presented in sections 4.1.1, 5 and 7.1.

3. Wavelets and T_e Resolution

[9] As will be seen from the synthetic model results in this paper, low-T_e features are better recovered than high-T_e features when using the fan wavelet method. This contrast between T_e estimation in strong and weak plates can be explained by considering both the nature of wavelets and the assumptions we make when inverting the wavelet coherence.

3.1. Wavelet Transform

[10] The CWT is a convolution of a space($\mathbf{x}$)-domain signal, say $g(\mathbf{x})$, with the complex conjugates of a family of scaled wavelets, ψ:

$$\tilde{g}(s, \mathbf{x}, \theta) = g(\mathbf{x}) * \psi^*_{s\theta}(\mathbf{x}) \quad (2)$$

where s is the scale of the wavelet, and θ is its azimuthal orientation (if the wavelet is anisotropic). The wavelet coefficients, $\tilde{g}(s, \mathbf{x}, \theta)$, contain, in essence, a localized amplitude/phase spectrum of the signal at each spatial location. The space dependence of the wavelet coefficients exists by virtue of the translation performed during convolution; their "frequency" dependence is revealed by the scaling of the wavelets.

[11] Importantly, wavelets must be localized in both space and wave number domains, but a "trade-off" exists between their precision in these domains, governed by a so-called "uncertainty relation":

$$\Delta\mathbf{x}\,\Delta\mathbf{k} \geq 2\pi \quad (3)$$

[e.g., *Addison*, 2002], where $\Delta\mathbf{x}$ is the precision or uncertainty of the wavelets in the space domain, and $\Delta\mathbf{k}$ is the precision in the wave number domain. This leads to an inverse proportionality between spatial and wave number precision. Large-scale wavelets are broad functions in the space domain, but have a narrow bandwidth; small-scale wavelets are spatially narrow and have a larger bandwidth (Figure 1). Hence, the large-scale wavelets capture a great deal of the signal, and while the corresponding wavelet coefficients accurately represent the long wavelengths of the signal, they tend to be spatially imprecise. Conversely, small-scale wavelets are highly localized, thus revealing the signal's short wavelengths, though these are smeared over adjacent wavelengths because of the larger bandwidth of these wavelets. Nevertheless, *Kirby* [2005] showed that if the Morlet wavelet is used, then the resulting wavelet power spectrum closely approximates the Fourier power spectrum (see also Appendix B1).

3.2. Coherence Transition

[12] However, the wavelet coherence method relies upon the analyzing wavelet at a certain scale being able to resolve the coherence transition wavelength (λ_t) in particular, defined as the wavelength at which the coherence has a value of $\frac{1}{2}$. We call those wavelets of such scale "transition wavelets." So in regions of high T_e when λ_t is large, the transition wavelets will be large-scale and will have been convolved with a great deal of the data. This means that data from surrounding regions with a low T_e will "contaminate" the wavelet coherence, at least over areas close to an appreciable change in T_e. Thus, if the high-T_e region is too narrow for the transition wavelets to exclusively cover it, then the recovered T_e there will be underestimated. This underestimation will be less pronounced in regions where the T_e contrast is small, and particularly when the absolute value of T_e is

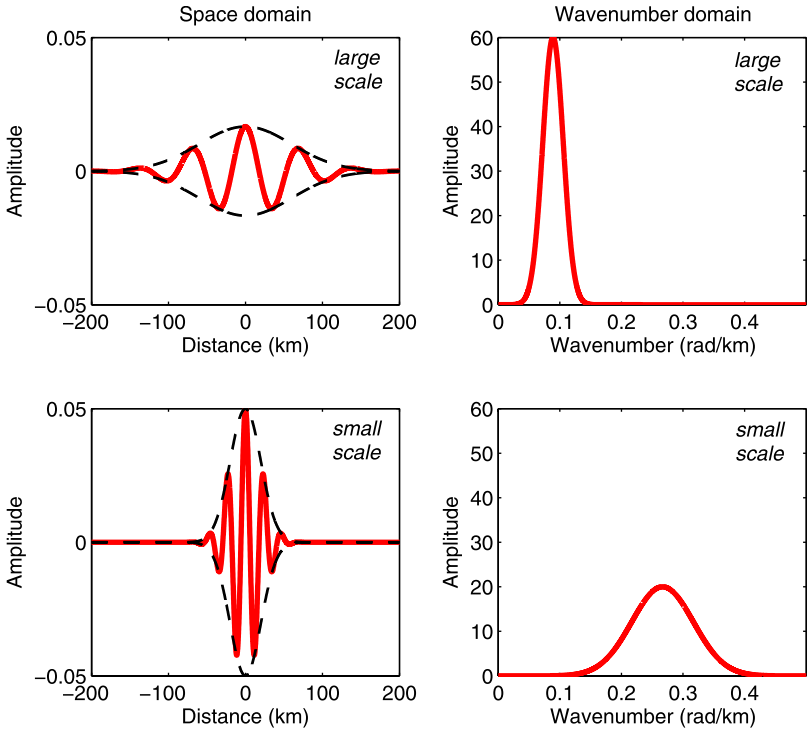

Figure 1. Cross sections through the 2-D Morlet wavelet at large and small scales, in the (left) space domain (real part) and (right) wave number domain. Dashed black line is the Gaussian envelope.

low, since the transition wavelets will be of small spatial extent because of a lower λ_t here.

[13] To quantify these effects we derive an algebraic equation relating both T_e and f to transition wavelet width. For the wavelet width, we use the diameter of the Gaussian envelope of the Morlet wavelet in the space domain at that particular scale/wavelength (equation (B5)). For λ_t, we obtain its expression as a function of T_e and f from the solution to the quartic equation describing half-coherence (Appendix D).

[14] Figure 2 shows a plot of the wavelet width needed to resolve a given T_e, for three different values of f. The factor p is the fraction of the maximum amplitude of the wavelet at a given scale ($0 < p < 1$) (Appendix B1). In this study, we use the $p = 0.01$ width of the Gaussian envelope (rather than, say, its $p = 0.5$ width) since this describes almost the full spatial extent of the wavelet (99.8% of its area), and hence gives a proper representation of the amount of data it is convolved with. As expected, the plot shows that the wavelet width must increase as T_e increases in order to resolve the large λ_t. However, it can also be seen that when f is very high then a smaller wavelet can successfully resolve a given T_e (see Appendix D).

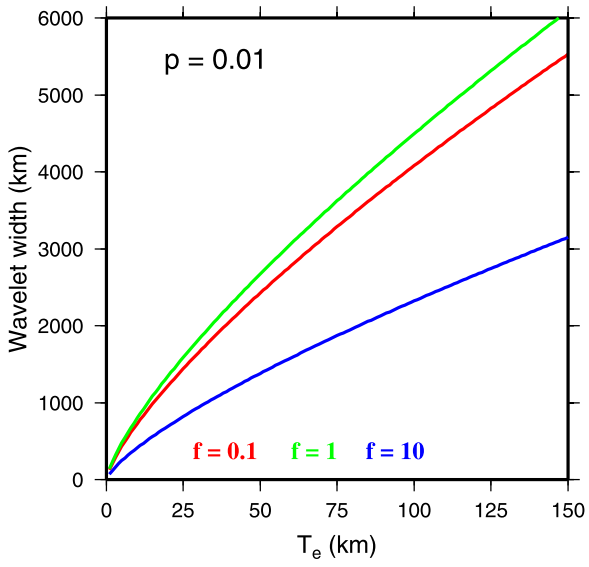

Figure 2. The width of the Gaussian envelope of the transition (Morlet) wavelet in the space domain, at a fraction $p = 0.01$ of the maximum wavelet amplitude, as a function of T_e, and for three different values of the loading ratio, f. The curves were computed using equation (B5), with λ_t obtained from the solution to equation (D5).

[15] In practice, it is advisable to choose the highest and lowest wavelet scale such that the transition wavelets have scales in the midwavelengths, where the uncertainty relation gives them optimal space and frequency domain precision. While this choice depends upon the dimensions of the study area and its grid spacing, the study area size does still need to be large enough to accommodate the spatial extent of the necessary transition wavelets (given the expected T_e in the region), else the recovered T_e will be underestimated. The maximum wavelet scale we use is of the order of the area dimensions, which limits the scale and spatial width of the transition wavelets, and hence limits the maximum possible recovered T_e. The effect of choosing a small study area upon T_e estimation with the fan wavelet method is shown in section 7.4.

3.3. Other Spectral Methods

[16] All the above effects are similar to bias experienced in multitaper methods [e.g., *Simons et al.*, 2000; *Swain and Kirby*, 2003; *Pérez-Gussinyé et al.*, 2004], where the recovered T_e is underestimated when the window size is too small for the transition wavelength to be faithfully resolved. And while *Macario et al.* [1995] found that decreasing window size led to an overestimated T_e, this is most likely due to the mirrored periodogram method they used, rather than the window size (see section 6). It is important to remember that, when used to recover spatial variations in T_e, the multitaper method divides the study area into subsets, or "windows," with a single coherence/admittance estimate computed for each window: the window size is chosen somewhat arbitrarily. The wavelet method, in contrast, does not need to use such "moving windows" because the wavelets sample all of the data in the study area at all scales at once, yielding local spectra at each grid node.

[17] Furthermore, space domain convolution methods [e.g., *Braitenberg et al.*, 2002] will also be affected by the magnitude of the transition wavelength. High-T_e features have a large flexural wavelength, which is a physical parameter, and not an artifact of the spectral methods. Hence, a very broad convolution kernel (the isostatic response function) is needed to faithfully reproduce these large flexural "depressions." Convolution with such a broad kernel in the space domain will lead to a smoothed signal, just as in the spectral methods. Hence, space domain convolution also needs large windows or data areas, if T_e is large in the study area.

3.4. Decoupling and Uniform T_e Assumptions

[18] Both the uniform f wavelet method and the wavelet-Forsyth method assume the independence of adjacent spectra: the "decoupling assumption" [*Stark et al.*, 2003; *Kirby and Swain*, 2004; *Swain and Kirby*, 2006]. This enables the inversion of the observed wavelet coherence at each grid node independently of the coherence at neighboring nodes. Of course, as discussed above, we expect a degree of coupling between the wavelet transforms at adjacent nodes due to the finite spatial extent of the wavelets.

[19] A separate assumption is made by load-deconvolution methods that T_e is uniform, so that the load equations can be formulated in the wave number domain where they are linear. These assumptions have some implications for the method which are explored in section 8.

4. Elliptical T_e Structures

4.1. Wide Plateau

[20] Figure 3a shows a "tectonic plate" comprising an elliptical plateau of T_e = 110 km (major axis 2400 km, minor axis 1200 km) smoothly dropping (over a ramp distance of 600 km) to a plain of T_e = 20 km. One hundred pairs of initial fractal loads were then emplaced upon this plate, yielding 100 final gravity/topography pairs. Each pair was then inverted using the fan wavelet method for its recovered T_e.

4.1.1. Mixed Versus Land Loading

[21] Figure 3b shows the result of inverting a gravity/topography pair generated from one particular random seed (005), when continental topography formed the load on the input T_e distribution ("land-loading"). Figure 3c shows the result (from a gravity/topography pair generated from the same random seed, 005) when the finite difference equations that generate the gravity/topography pair take into account the fact that some regions are underwater. As discussed in section 2.2, the mixed-loading case gives a slightly better recovery (in terms of T_e magnitude) than with land-only loading. This is confirmed by the statistics (section 4.1.3) for the fit between the input and recovered models and also by

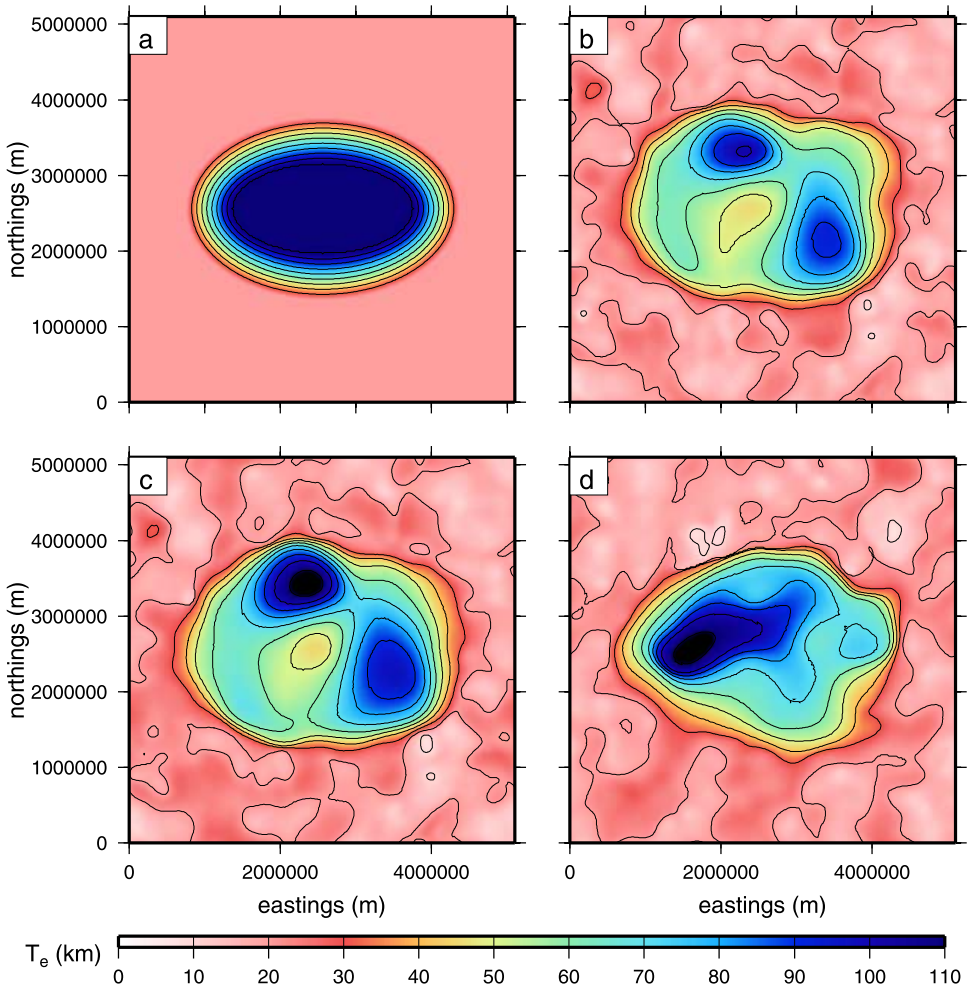

Figure 3. (a) Model T_e distribution. (b) Recovered T_e from model 005 (land loading). (c) Recovered T_e from model 005 (mixed loading). (d) Recovered T_e from model 033 (mixed loading).

the other models considered (e.g., Figure 8c). Importantly though, the slight differences between Figures 3b and 3c show that the mixed-loading flexure equations are a reasonable approximation, and that the equivalent topography and land-loading equations are applicable to real-Earth situations.

4.1.2. Random Correlations

[22] Figure 3d shows the recovered T_e from another random seed (033). It is evident that, even though the model T_e is the same, the different random fractal loads are generating significant differences in the recovered elastic thicknesses. To investigate why this should be so, we turned to the fractal surfaces used as initial loads on the plate. Recall, the coherence method [*Forsyth*, 1985] is applicable only under the assumption that the surface and subsurface loads are statistically uncorrelated. However, owing to the inherent nature of the fractal surface generation method, random correlations between the two surfaces often arise, and as noted by *Macario et al.* [1995] any increase in correlation lowers the recovered T_e.

[23] To investigate the nature of these random correlations, we calculated the wavelet coherence between all 100 fractal surface pairs that were used as initial loads. Figure 4 shows results for two out of the 100 models (005 and 015). Figure 4 (top) shows north-south profiles at 2560 km easting from the recovered T_e in each case, and it can be seen that they show large differences. Figure 4 (middle) shows slices through the wavelet coherence between the initial loads at 2560 km easting. Figure 4 (bottom) shows such slices through the observed wavelet coherence between the final gravity/topography after loading. Of immediate

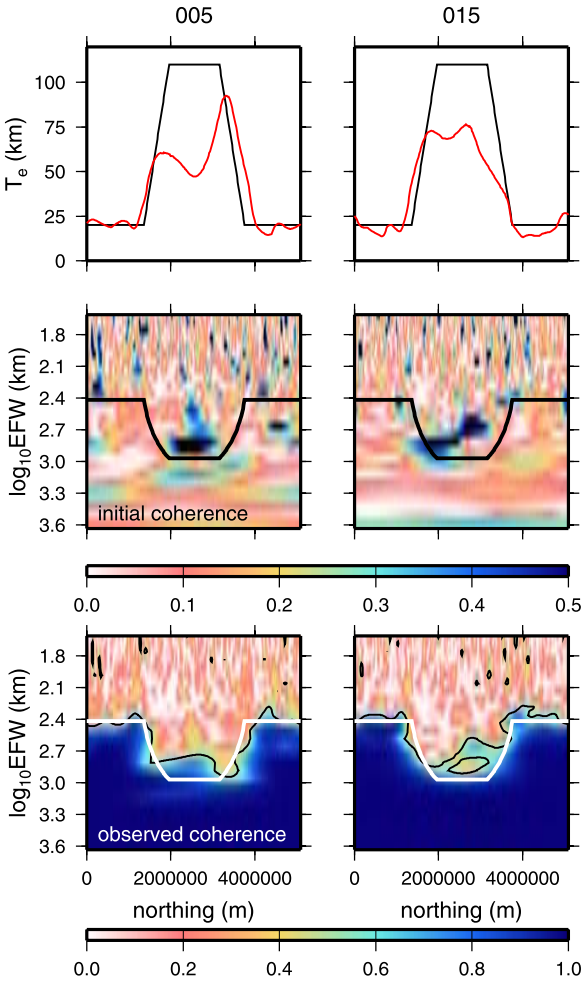

Figure 4. Coherence of the loads before and after (land-only) loading on the elliptical T_e structure in Figure 3a, for two individual models (005 and 015). (top) Profiles extracted from the recovered T_e at 2560 km easting (red), together with a similar profile extracted from the model T_e in Figure 3a (black). (middle) Wavelet coherence between the initial loads at 2560 km easting (EFW is equivalent Fourier wavelength) and (bottom) wavelet coherence between the final gravity and topography at the same easting. The half-coherence contour is plotted in black in Figure 4 (bottom). The thicker black and white lines in the coherence plots mark the location of the coherence transition wavelengths for the model T_e from equation (D5) for $f = 1$. Color scale in Figure 4 (middle and bottom) is coherence, but note the difference between these scales.

concern are the incidences of high coherence between the initial loads, which occur at random spatial locations and wavelengths, and reach magnitudes of over 0.5. Remember, the coherence method requires zero coherence everywhere between the initial loads, and it seems that even setting Macario's correlation coefficient to zero (as we did) does not remove these random correlations. The black and white lines in Figure 4 (middle and bottom) indicate the coherence transition wavelength of the T_e model, which we would expect to mark out the contour of 0.5 coherence. However, Figure 4 shows that the observed half-coherence contour is generally at wavelengths less than the flexural wavelength, implying an underestimated T_e.

[24] The effect of these initial load correlations upon the final gravity/topography coherence is readily apparent in Figure 4. The areas of high initial load coherence map directly into high final coherence at the same wavelength/location, and serve to increase the final coherence. This increase in final coherence results in a reduced T_e upon inversion. Again, this phenomenon is seen by comparing the T_e profiles for each model with the regions of anomalous initial coherence: the T_e anomalies can largely be mapped back to initial load coherence anomalies around the flexural wavelength. Note that initial coherence anomalies far from the transition wavelength do not corrupt the inversion.

[25] Averaging the individual coherences between each of the 100 initial load pairs gives a "background coherence." This averaged coherence has a mean value of 0.18 (and not zero, as it should be), with minimum and maximum values of 0.1 and 0.34, respectively.

[26] To properly assess the recovery accuracy of the wavelet method, the random correlations between initial loads should be removed, or at least reduced. Therefore we computed the recovered T_e from each of 100 synthetic model pairs and averaged these T_e grids. This gives an assessment of the method that is independent of the particular initial fractal load pair and their random correlations.

4.1.3. Results

[27] The averaged recovered T_e for the mixed-loading case is shown in Figure 5f. The overall misfit between the model and recovered average T_e is 3.0 ± 10.2 km (mean difference ± difference standard deviation). We do not show the result for the land-only loading case because it is very similar, showing a difference of 4.3± 10.3 km with the model T_e. The slightly better recovery capability of the mixed-loading case is discussed in section 4.1.1. Note that the recovered T_e is very

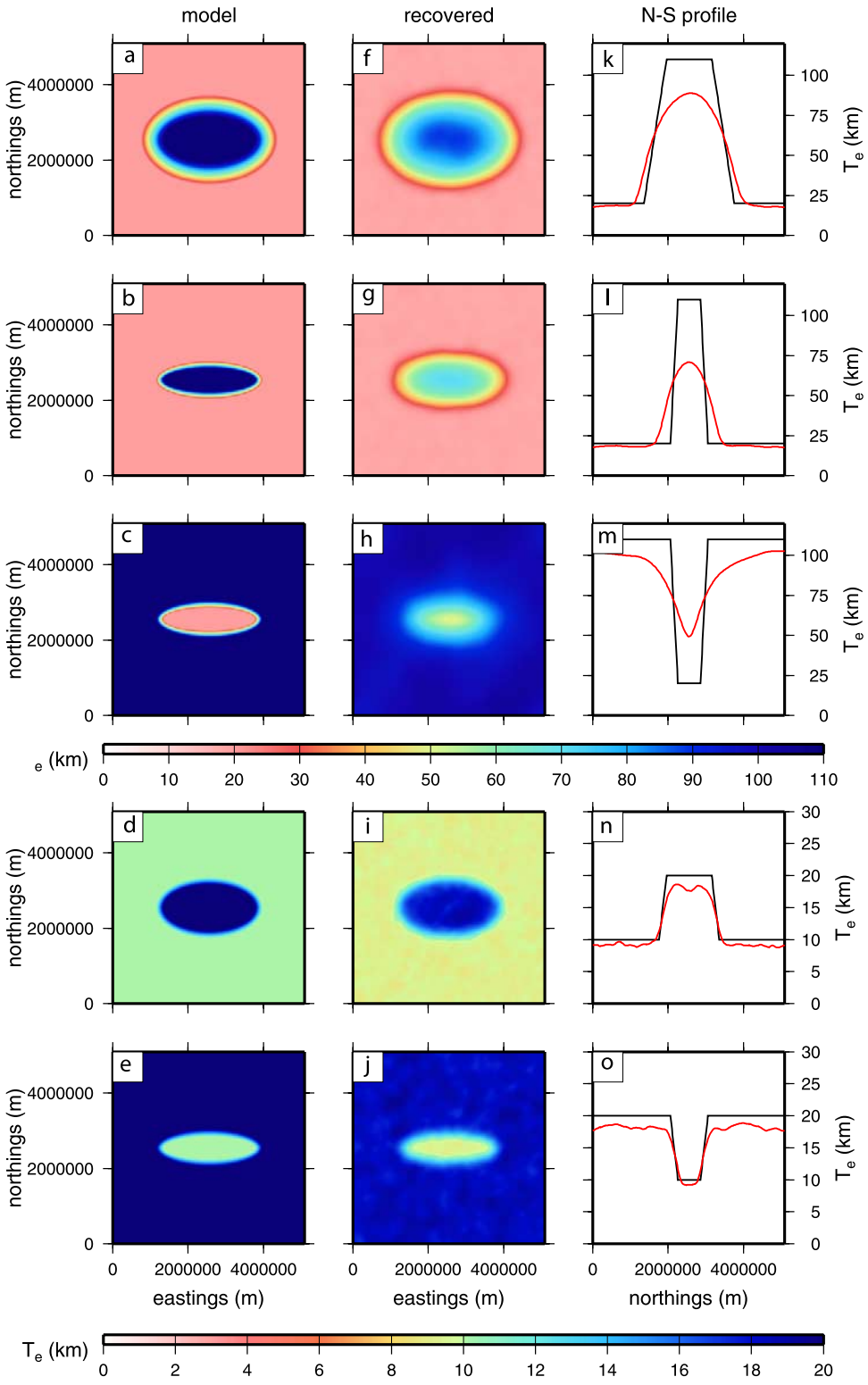

Figure 5. Elliptical T_e recovery. (a–e) Model T_e, (f–j) averaged recovered T_e (over 100 results), and (k–o) north-south cross sections, at 2560 km easting, of the model (black) and average recovered (red) T_e. All mixed loading.

smooth, with minimal evidence of the higher-frequency anomalies present in Figures 3b–3d that arise from the random correlations.

[28] Figure 5f shows that the wavelet method has underestimated the higher-T_e part of the model, though Figure 5k shows more detail, being a north-south cross section through the model and recovered average T_e at 2560 km easting. Generally, the recovered T_e is flattened (by approximately 20 km at the plateau center), and broadened (by approximately 300 km either side of the plateau base), though the overall elliptical shape is preserved. From Figure 2, a region with T_e = 110 km needs a transition wavelet of width ~5000 km for its successful resolution (for f = 1), going some way to explaining the diminished recovered amplitude of the plateau, whose minor axis is only 1200 km. In the T_e = 20 km plain away from the ellipse, the recovery is good, to within 2 km.

4.2. Other Elliptical Structures

[29] The results for the recovery from other elliptical T_e distributions are shown in Figure 5, where the structure width and T_e magnitude has been varied. Figures 5b, 5g, and 5l show how the recovery degrades when the minor axis in Figure 5a is decreased, because the transition wavelet width is now significantly greater than the anomaly width, and more information from the surrounding (low-T_e) region is included in the wavelet coefficients, and therefore coherence. Figures 5c, 5h, and 5m show the effect of reversing the structure in Figure 5b. In this case the recovered structure is not simply the reverse of the recovered structure in Figure 5g, because the surrounding large-width T_e = 110 km transition wavelets are contaminating the recovery of the ellipse. Hence, rather than T_e being underestimated by the fan wavelet method, we should say that it is relative T_e differences that are underestimated.

[30] While the recovery of the high-T_e model was good, but not ideal, that of a low-T_e feature is much better. In contrast to T_e = 110 km, the transition wavelets for T_e = 20 km are only of width ≈1400 km, explaining why the T_e = 20 km ellipse in Figure 5i is better resolved in both spatial extent and in T_e magnitude than its counterpart in Figure 5f. Both ellipses have a minor axis of 1200 km, which is less than the transition wavelet width for T_e = 110 km, but is of the same order as the transition wavelet width for T_e = 20 km. Furthermore, the recovery is also good for a reversed model with a narrower ellipse, shown in Figures 5e, 5j, and 5o.

[31] Note that the T_e recovery in Figures 5i and 5j shows much more short-wavelength variation than the higher T_e results (see the cross sections in Figure 5). This is because when the transition wavelength is longer, the transition wavelets are large-scale and spatially wide, and the resulting coherence is spatially smoothed out. This phenomenon is visible in all wavelet transform power spectra, and can be seen in Figure 4 (middle), where the long-wavelength coherence contains much less spatial detail than does the short-wavelength coherence.

5. Uniform T_e Plates

[32] The above results for the T_e ellipses show an underestimation of T_e of around 10–20%, depending upon (1) the spatial location relative to the high-T_e ellipse and (2) the absolute and relative T_e values. However, by applying the procedure to plates with a uniform T_e distribution, it is possible to remove the dependence of the recovery upon T_e anomaly width and relative amplitude, and thus estimate a "background" underestimation or overestimation percentage due to other effects. To this end, we computed 100 gravity/topography pairs (setting f = 1) for plates with a range of uniform T_e values, from 10 km to 150 km, and attempted to recover the model T_e in each case. We performed these computations on synthetic models generated from both mixed and land loading.

[33] The percentage difference between the model and average recovered T_e, relative to the model T_e, is shown in Figure 6. For both mixed and land loading, as T_e increases its recovered value becomes more underestimated, but the amount of underestimation is relatively constant and independent of T_e. This also applies to the standard deviations. For mixed loading, the mean underestimation is approximately 8.7% of the true T_e, while the mean error is approximately 1.6% of the true T_e. For land loading, these statistics are 11.8 ± 1.5%, which supports our finding that use of the mixed-loading inversion equations with equivalent topography provides slight upward biases in T_e (Appendix C3).

[34] That these uniform plates have no T_e anomalies, yet still show an underestimation, points to a second reason for the T_e underestimation we observe, and one that does not involve transition wavelet widths. We believe that this inherent underestimation of T_e for synthetic models is due

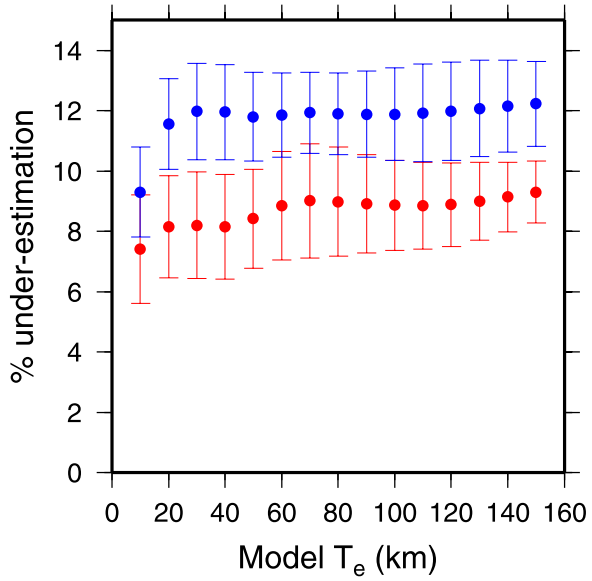

Figure 6. Uniform T_e recovery ($f = 1$, 5100 × 5100 km area), showing the difference between the average recovered and model values, as a percentage of the model [$100(T_e^{\mathrm{mod}} - T_e^{\mathrm{rec}})/T_e^{\mathrm{mod}}$]. Error bars are one standard deviation of the percentage difference (=$100\ \sigma_{T_e^{\mathrm{rec}}}/T_e^{\mathrm{mod}}$, from propagation of variances). The red symbols are from mixed-loading synthetic models, and the blue symbols are from land-only models.

to the nonzero coherence between initial loads at random wavelengths and spatial locations, as discussed in section 4.1.2, and will apply to all T_e recovery experiments on synthetic models. It is difficult to quantify the exact effect of this background coherence, but we reason that it will serve to increase the final coherence at the transition wavelength by a small but significant amount, thus providing an underestimate of T_e. To support this conclusion, we note that *Macario et al.* [1995] reported a general decrease in the recovered T_e as the correlation coefficient between the synthetic loads was increased, though there is no consistency to their difference percentages like those we observe.

[35] However, we note that it is likely that the specific value of this underestimation percentage will depend upon both the analysis method and the study area dimensions, and the value of 8.7% (11.8%) that we observe applies only to this particular analysis.

6. Effect of Mirroring

[36] The preprocessing technique of mirroring the gravity/topography data before performing a Fourier transform has been performed in many studies [e.g., *Zuber et al.*, 1989; *Lowry and Smith*, 1994; *Macario et al.*, 1995; *Hartley et al.*, 1996; *McKenzie and Fairhead*, 1997; *Poudjom Djomani et al.*, 1999; *Ojeda and Whitman*, 2002; *Stephen et al.*, 2003; *Stark et al.*, 2003]. Authors using mirroring with Fourier-based coherence methods, such as periodogram, maximum entropy and multitaper methods, have reported that the recovered T_e is usually overestimated when mirroring is performed [e.g., *Lowry and Smith*, 1994; *Ojeda and Whitman*, 2002; *Stephen et al.*, 2003]. The mirroring introduces artificial long-wavelength signals into the data, which have the effect of shifting the coherence transition to smaller wave numbers [*Lowry and Smith*, 1994; *McKenzie and Fairhead*, 1997; *Ojeda and Whitman*, 2002]. However, *Stark et al.* [2003] used mirroring with their wavelet method, and found less of a problem. This difference with the Fourier results, they said, was because the wavelets are localized in both space and wave number domains and thus the artificial wavelengths do not contaminate the entire signal, as they do with Fourier methods.

[37] Here we investigate the effect of mirroring upon wavelet T_e recovery. Figure 7a shows the same ellipse as in Figure 5a, but moved to the area edge, and with a circular plateau (diameter 600 km) also of magnitude T_e = 110 km, dropping sharply (over a distance of 100 km) to T_e = 20 km on the plain. The averaged recovered T_e when the synthetic data were not mirrored about their edges is shown in Figure 7b, while Figure 7c shows the result when they were mirrored.

[38] Figure 7b shows that if this mirroring is not performed, then the high T_e plateau on the western edge becomes "wrapped around," appearing also on the eastern edge. This phenomenon is not an artifact of the periodic boundary conditions assumed in the flexure algorithm, because if it were, then a high T_e would also be recovered on the right-hand edge with the mirrored data (Figure 7c). Therefore, mirroring has the effect of avoiding T_e wraparound when a high-T_e structure abuts the edge of the data area. This wrapping occurs at the Fourier transform stage of the wavelet transformation (or equivalently, in the convolution), when the data grids are juxtaposed without mirroring, and the transition wavelets "map" the high T_e onto the opposite side. While mirroring removes this phenomenon, if possible the study area should be chosen so that high-T_e structures are more centrally located.

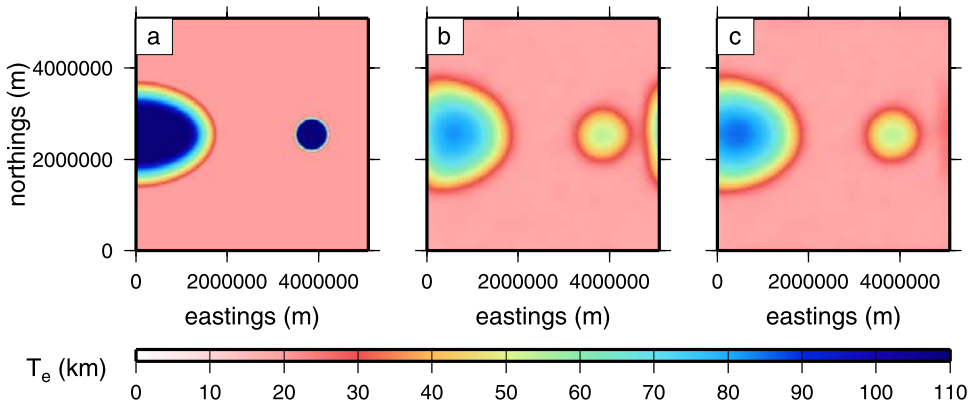

Figure 7. (a) Model T_e distribution. (b and c) Recovered T_e from average of 100 models, computed without and with mirroring of the gravity/topography data, respectively (mixed loading).

[39] We agree with *Stark et al.* [2003], finding very little difference between the unmirrored and mirrored elastic thicknesses in the central areas of Figures 7b and 7c, and also no difference between the elliptical part of the elastic thicknesses in Figures 5f and 7c, taking into account the shift in the ellipse. However, note that the gravity/topography grids in this particular analysis are periodic and that the study areas are relatively large: in sections 7.3 and 7.4 we address the case of mirroring nonperiodic data over smaller areas.

[40] Comparison of Figure 7c with 7a shows that although the small circular feature has clearly been retrieved, both its amplitude and gradient are greatly reduced. The reason is that the wavelets cannot fully resolve it, as its diameter is much smaller than even the $p = 0.5$ width of the $T_e = 110$ km transition wavelet. However, a similar phenomenon occurs with sharp, circular $T_e = 5$ km zones of diameter 400 km, which we would expect to be recovered well because this diameter is greater than the $p = 0.1$ wavelet width. In this case the problem can be attributed to failure of the decoupling assumption (section 3.4). This supposes that adjacent spectra are independent whereas in fact they are not, and for steep T_e gradients this can lead to complexities in the 3-D coherence and hence to distortion of the recovered T_e distribution. The effect of steep T_e gradients upon its recovery is explored further in section 8. However we have not found it to be a serious shortcoming of the method if the T_e gradients are not too large.

7. Fractal T_e Structures

[41] As a further test of the wavelet coherence method, we attempted to recover an elastic thickness from synthetic gravity/topography data generated from loading of a plate with a fractal T_e distribution. Whereas the application to geometrically shaped T_e distributions described above is a useful indicator of the method's recovery accuracy, fractal T_e distributions are likely to be closer to the real Earth's T_e structure. We used the spectral synthesis method of *Peitgen and Saupe* [1988] with a fractal dimension of 2.0 to generate the distributions shown in Figure 8a ("fractal 1"), and Figure 9a ("fractal 2"). The spatial dimensions of the grids were 8620 × 8620 km for fractal 1, and 10,220 × 10,220 km for fractal 2.

7.1. Wave Number–Independent Loading Ratio

[42] As a first test, the initial loads were given equal fractal dimensions of 2.5. For fractal 1 we tested both land-only and mixed loading, while for fractal 2 we used land-only loading.

[43] Figure 8b shows the averaged recovered T_e for fractal 1, while Figure 9b shows that for fractal 2. It is evident that the long-wavelength structure of the models has been recovered well in both cases, while the short-wavelength T_e variations have been smoothed to a degree proportional to the absolute value of T_e in the locality. This effect has been discussed in sections 3 and 5, and is also illustrated in Figure 8c, which shows cross sections through the model (black curve) and average recovered T_es (red curve) for fractal 1. Again, high-T_e anomalies are more underestimated, because of their width being less than the transition wavelet width. As seen before (section 4.1) the mixed-loading case gives a slightly better recovered T_e than land-only loading (blue curve in Figure 8c), with the misfits

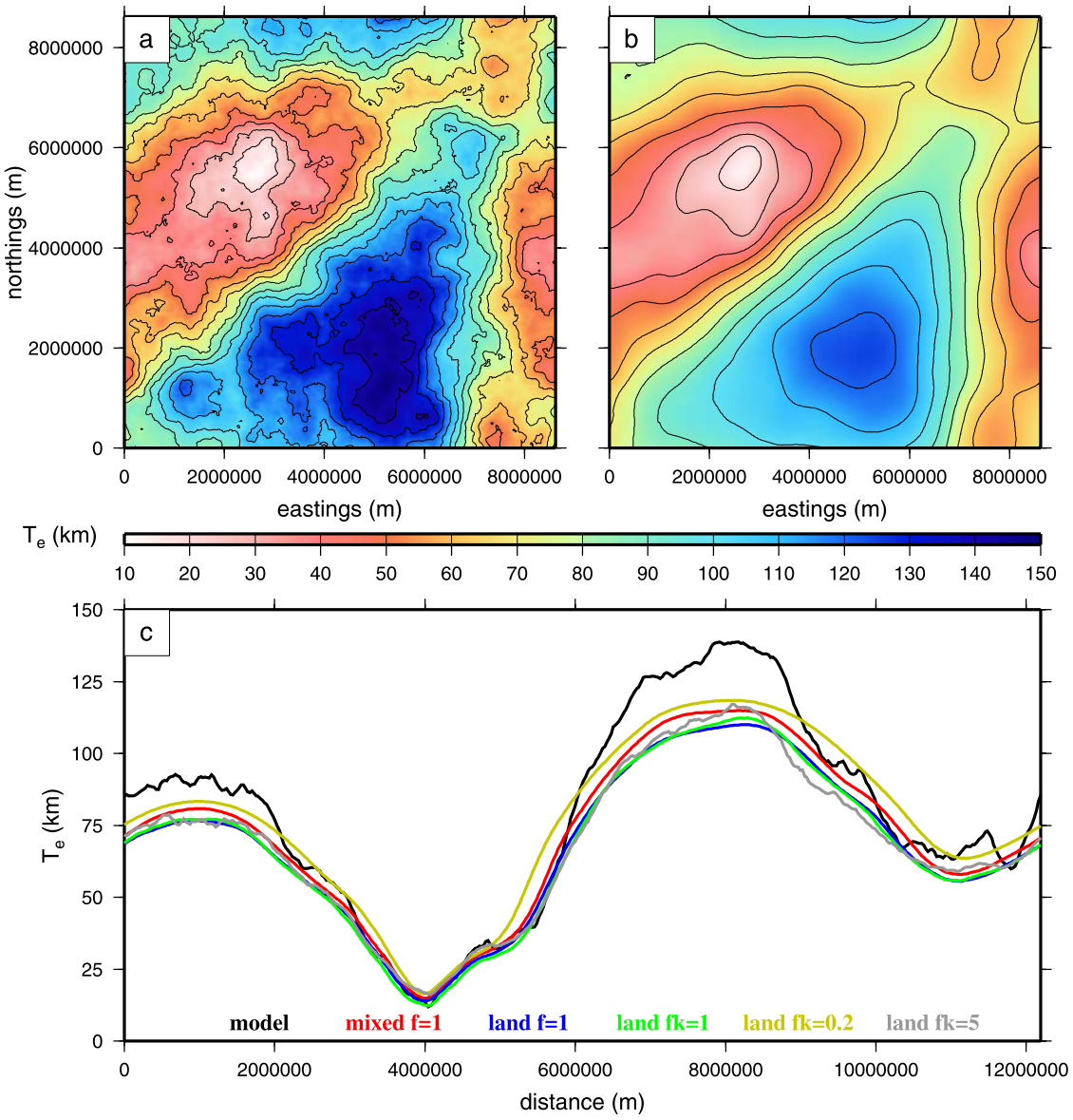

Figure 8. (a) Model T_e distribution ("fractal 1"). (b) Recovered T_e from average of 100 models (mixed loading). (c) Cross sections, from the northwest to southeast corners, from the T_e grids in Figures 8a and 8b (black and red, respectively), and from four other grids (see section 7.2 and figure legend). In the legend, the "f" indicates loading ratio for surface/subsurface load fractal dimensions of 2.5/2.5 (i.e., uniform f), while the "fk" indicates loading ratio for a fractal dimension of 2.5/3 (i.e., wave number–dependent f; see section 7.2).

being 7.4 ± 7.9 km for the former, and 10.5 ± 8.4 km for the latter.

7.2. Wave Number–Dependent Loading Ratio

[44] There has been some debate in the literature recently concerning the T_e recovery ability of the Bouguer coherence method in regions where erosion has greatly reduced the topographic amplitude [*McKenzie and Fairhead*, 1997; *McKenzie*, 2003]. In an attempt to show that this method is still effective in such regions, *Swain and Kirby* [2003] and *Swain and Kirby* [2006] performed synthetic modeling, using multitapers and wavelets respectively, on gravity/topography pairs where the initial loads had fractal dimensions of 2.5 (surface) and 3.0 (subsurface). This difference in fractal dimension has the effect of (1) inducing a wave number (k) dependence in the loading ratio (Appendix A) and (2) reducing the power in the "uncompensated topography" to below that of the free-air gravity

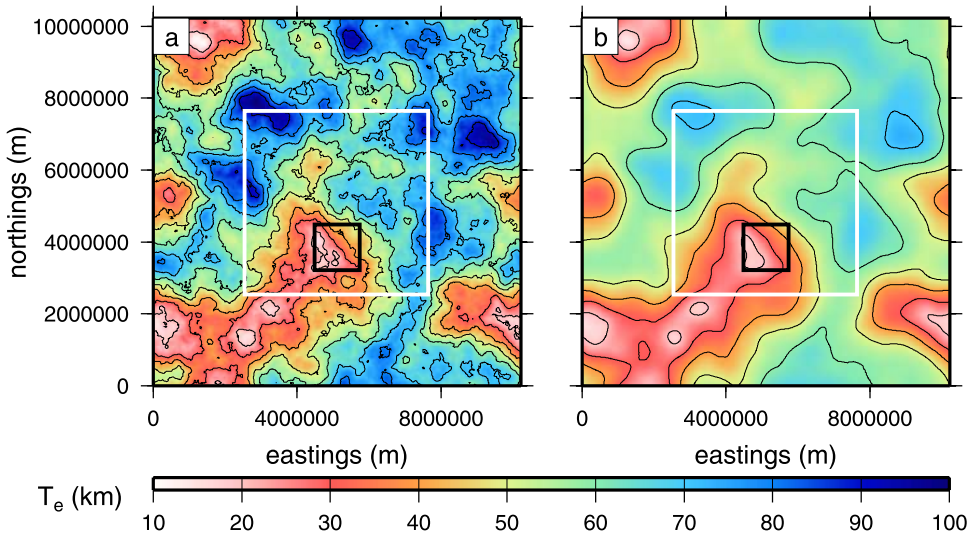

Figure 9. (a) Model T_e distribution ("fractal 2"). (b) Recovered T_e from average of 100 models (land loading). The white boxes show the extents of subset 1 (Figure 10), and the black boxes show the extents of subset 2 (Figure 11).

anomaly [*Swain and Kirby*, 2003]. Recall, *McKenzie and Fairhead* [1997] postulated that when this latter scenario occurs, whether through erosion or large amplitude subsurface loads without topographic expression, then the Bouguer coherence method returns overestimates of the true T_e.

[45] Hence, we generated 100 gravity/topography pairs for the fractal T_e model 1, using the land-only loading model, and with initial surface and subsurface loads having fractal dimensions of 2.5 and 3, respectively. We tested three cases of the (wave number–dependent) loading ratio: $f(k_t) = 0.2$ representing predominantly surface loading, $f(k_t) = 1$ representing equal surface and subsurface loading, and $f(k_t) = 5$ representing predominantly subsurface loading. Note that these f values indicate the loading ratio around the coherence transition wave number (k_t), whereas the different fractal dimensions imply a wave number–dependent loading ratio.

[46] The maps of the average recovered T_e for each case look very similar to that in Figure 8b, so instead of presenting these, in Figure 8c we show cross sections from the three results (see figure caption and legend). Generally, all profiles have very similar values, indicating that the recovery ability of the fan wavelet coherence method is largely independent of the loading environment, and that, with this method, T_e is still underestimated, and not overestimated as *McKenzie and Fairhead* [1997] claim.

[47] The $f(k_t) = 5$ recovery contains more high-frequency content in T_e (which matches the high frequencies in the model) because the transition wavelength for $f = 5$ is at shorter wavelengths than for smaller values of f at the same T_e [*Forsyth*, 1985], meaning the transition wavelets are smaller-scale with better spatial resolution (Figure 2). The $f(k_t) = 0.2$ profile gives the best recovery in an absolute sense, but is much smoother than the others for the same reason.

7.3. Nonperiodic Loads

[48] All the synthetic gravity/topography models discussed so far were generated using periodic boundary conditions in the flexure algorithm. This means that there will be no discontinuities in the signal or its gradient between opposite edges of the data area, yielding no edge effects when Fourier transformed. However, this periodicity does not occur with real data. Therefore, to simulate real, nonperiodic gravity/topography data, we extracted two subsets from each of the 100 gravity/topography grids generated from fractal 2. These subsets are shown as the white and black boxes in Figure 9a.

[49] Figure 10a shows the extracted T_e distribution over subset 1, with dimensions 5100 × 5100 km. Figure 10b shows the averaged (over 100 results) recovered T_e, when the gravity/topography data extracted from the whole area were not mirrored, while Figure 10c shows the result with mirroring. There are considerable edge effects arising from Fourier transformation of nonperiodic data without

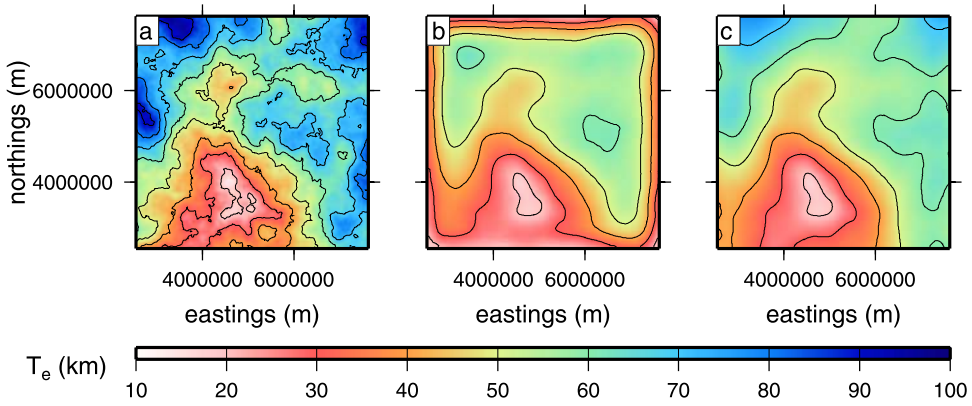

Figure 10. (a) Model T_e distribution (subset 1, extracted from white box in Figure 9a). (b and c) Average recovered T_e from gravity/topography extracted over subset 1, without and with mirroring, respectively.

mirroring, and only the low-T_e anomalies toward the center of the area are recovered well. Mirroring of the data, however, has removed the edge effects to the extent that the recovered average is now very similar to the model T_e. Note though, that the high-T_e features are still underestimated, as has happened with all our synthetic results.

[50] From this particular analysis, we conclude that mirroring of real (i.e., nonperiodic) gravity/topography data should invariably be performed prior to T_e estimation with the wavelet method, or at least performed alongside an unmirrored version.

7.4. Small Area

[51] Figure 11a shows the extracted T_e distribution over subset 2, where the elastic thickness is generally low. This box has dimensions 1260 × 1260 km. Figure 11b shows the averaged recovered T_e with mirroring. There is a reasonable recovery of T_e, though its gradient is reduced in magnitude. For comparison, Figure 11c shows a magnification of the recovered T_e grid in the black box in Figure 9b, i.e., when the complete data set is used. While the T_e recovery from data limited to the smaller area compares well at longer wavelengths with the extracted values, there are differences, notably the reduced T_e gradient, and the lower values along the eastern edge.

[52] We conclude that, even with mirroring, the results when performed over a relatively small area are significantly worse than those obtained by using the extended data set.

8. A "Faulted" Fractal T_e

[53] In Figure 7c the amplitude and gradient of the small circular T_e anomaly was greatly underestimated, and two reasons were proposed to explain this (besides the background coherence bias). First, the diameter of the anomaly is much less that the

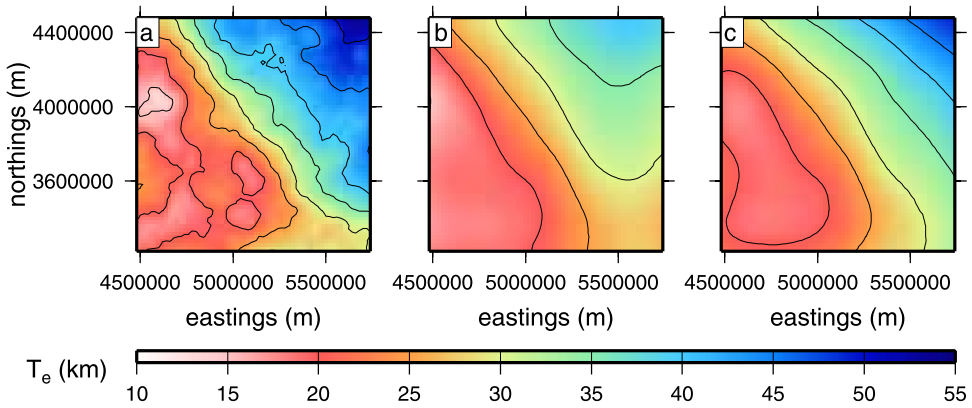

Figure 11. (a) Model T_e distribution (subset 2, extracted from black box in Figure 9a). (b) Average recovered T_e from inversion of (mirrored) gravity/topography data extracted over subset 2. (c) Average recovered T_e extracted directly from the black box in Figure 9b.

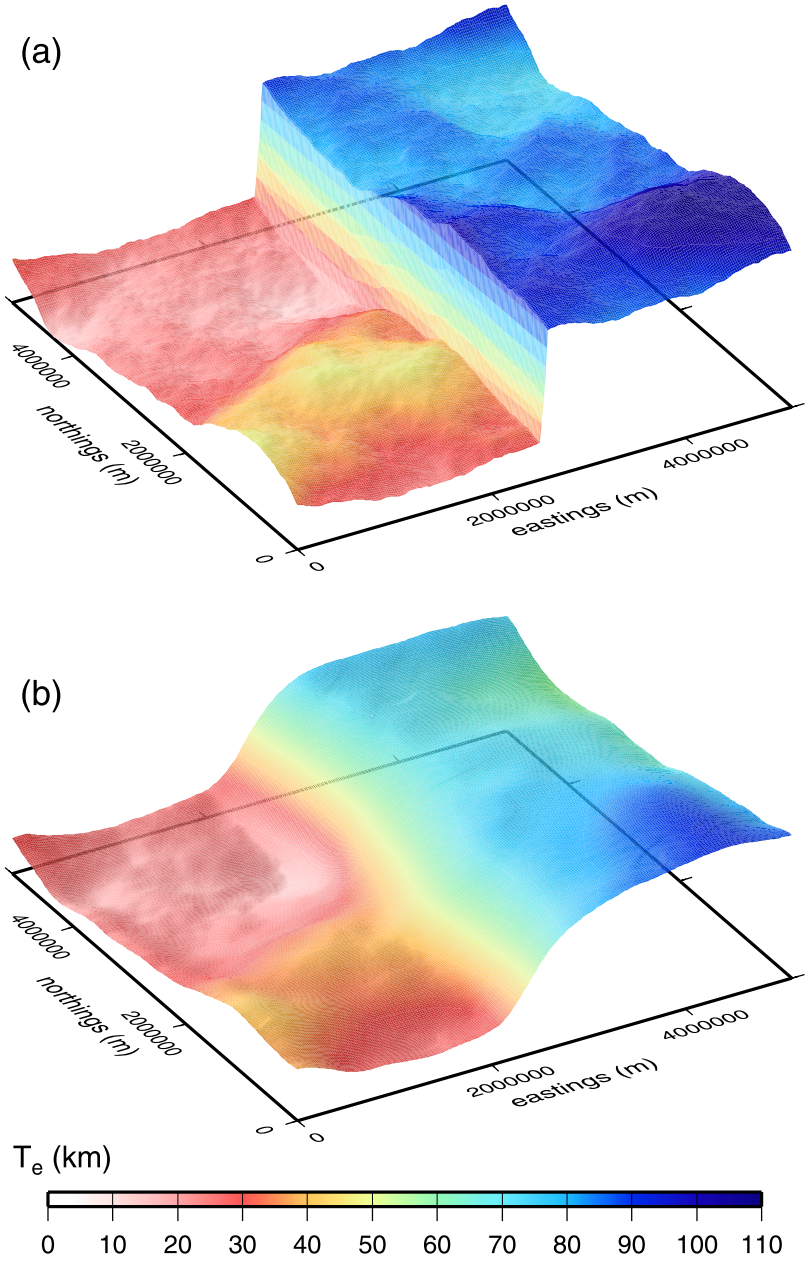

Figure 12. A faulted fractal T_e. (a) Model T_e distribution, being a fractal T_e with a 60 km "fault." (b) Average recovered T_e (land loading).

transition wavelet width. Second, the steepness of the T_e gradient could possibly invalidate the decoupling assumption in this region.

[54] In an attempt to separate these effects, we tested a plate with a fractal distribution (fractal dimension 2.0), but with a "fault" of magnitude 60 km and width 100 km splitting the area in half (Figure 12a) so that issues of transition wavelet width ought not to be as significant. The average recovered T_e (over 100 models, land-loading, mirrored gravity/topography) is shown in Figure 12b, and while the recovery is good, the steep T_e gradient across the fault has been reduced.

[55] Figure 13 (top) shows T_e profiles extracted from these grids at 2000 km and 4000 km northing. The reduced gradient of the recovery is obvious, particularly for the 2000 km profile where T_e is generally higher and the transition wavelets are broader. Over the fault, however, the observed coherence "gradient" (i.e., the gradient of the half-coherence locus in the eastings direction) is

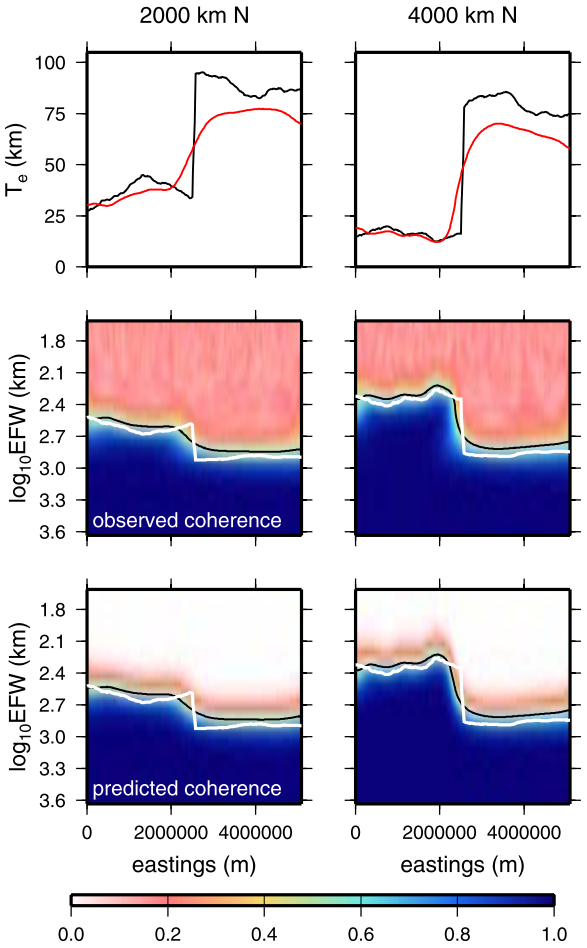

Figure 13. Cross sections through T_e and averaged coherences for the faulted fractal T_e model. (left) Profiles extracted at 2000 km northing and (right) profiles extracted at 4000 km northing. (top) Profiles extracted from the model T_e (black, Figure 12a) and average recovered T_e (red, Figure 12b). (middle) The 100-averaged observed and (bottom) predicted coherences. The white lines in the coherence plots mark the location of the coherence transition wavelengths for the model T_e from equation (D5) for f = 1, the half-coherence contour is plotted in black, EFW is equivalent Fourier wavelength, and color scale is coherence.

actually slightly sharper than the predicted coherence gradient over the fault.

[56] At first glance it would seem that the predicted coherence is not modeling the observed coherence over the fault as well as we might expect. However, plotting one-dimensional (1-D) coherence profiles along 4000 km northing (Figure 14) shows that this is not the case, and that the predicted coherence provides a good fit to the observed coherence, particularly at locations away from the fault. As the fault is approached from the west, the "blip" in the coherence rollover begins to move to higher wave numbers, until it almost disappears at the fault itself (2550 km easting). This blip is not visible in the high-T_e eastern regions, and is a consequence of the high-T_e signal leaking into the low-T_e western regions by virtue of the large transition wavelet width.

[57] Hence, we conclude that the major cause of reduced T_e gradients is coupling between adjacent wavelet spectra over a T_e discontinuity. This is evident in the observed coherence profiles in Figure 14. In contrast, the assumption of uniform T_e in the inversion (section 3.4) does not seem to be as significant, because the inversion does a fair job of predicting the observed coherence, irrespective of whether or not the observed coherence is truly representative of the actual T_e.

[58] (As a check on these results we also applied the uniform f method, using the theoretical coher-

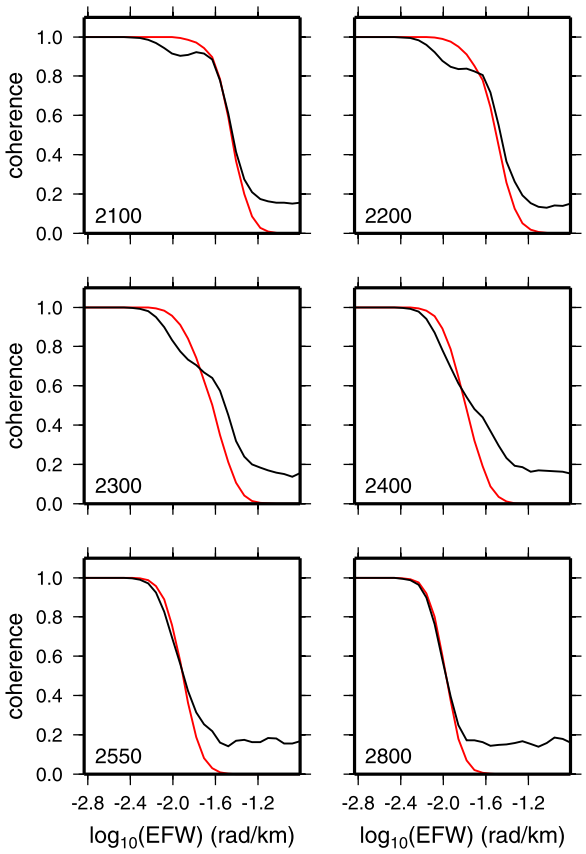

Figure 14. Average observed (black) and predicted (red) 1-D coherence profiles extracted from Figure 13 (right) (i.e., at 4000 km northing) at the easting (in km) indicated in each panel. The T_e "fault" lies at 2550 km easting. EFW is equivalent Fourier wave number.

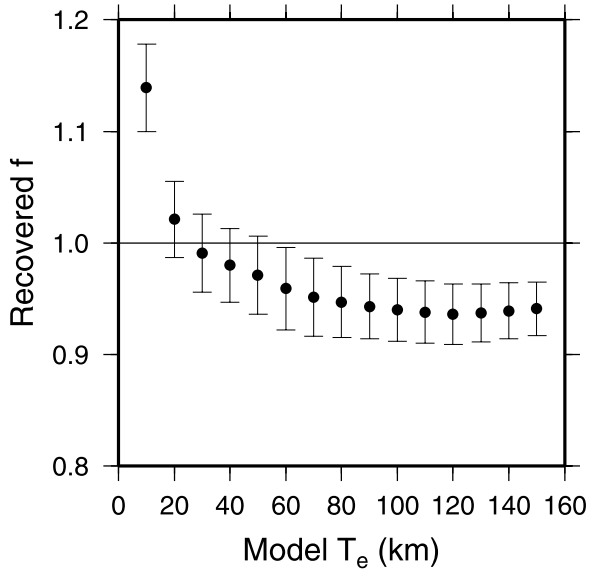

Figure 15. The recovered initial subsurface-to-surface loading ratio at the coherence transition wavelength [$f(k_t)$], averaged over 100 models and averaged over all grid nodes, for 15 uniform T_e plates (mixed loading). Error bars are one standard deviation of the 100-average, and the straight line plots $f = 1$, which is the value that the synthetic loads were given.

ence formula (equation (D1)) with $f = 1$ at all wave numbers. We obtained almost identical results for both coherence (predicted versus theoretical) and recovered T_e. As $f = 1$ in the model, this agreement is expected.)

[59] Interestingly, note the high–wave number average observed coherence asymptote in Figure 14 is ~0.2 and not zero, and recall that the average initial-load coherence for these models is 0.18 (section 4.1.2). This provides further evidence of the propagation of initial into final coherence in the synthetic method.

9. Estimation of the Loading Ratio

[60] The wavelet-Forsyth inversion method can, if desired, give the loading ratio between initial subsurface and surface loads (f, Appendix C1), which is a function of both spatial position and wave number (k). However, plots of this recovered f, such as in the fourth row of Figure 17, show a wave number dependence even if the initial loads have equal fractal dimension when we would expect to find $f(k) = 1$, $\forall k$ (see Appendix A). This observed increase of the recovered f with wave number is not peculiar to wavelet methods, though it is probably more marked because there is less averaging of the spectra at high wave numbers than with Fourier methods.

[61] Part of the discrepancy can be explained by the downward continuation of the Bouguer anomaly to the Moho in the Forsyth method (see equation (C6)), which overly amplifies the high–wave number components of the subsurface load spectrum, and forces an increase of recovered f with wave number. In support of this argument, performing the coherence inversion using a wavelet adaptation of the *Banks et al.* [2001] deconvolution method gives a relatively constant f (at least for shallow internal loads), because the (implied) downward continuation is to a shallower depth (see equation (C13)).

[62] The k dependence at low and intermediate wave numbers is not so easily explained. Nevertheless, we do observe a good recovery of f at the coherence transition wave number, $f(k_t)$. Figure 15 shows the averaged recovered $f(k_t)$ values for uniform plates with T_e varying from 10 to 150 km. For $T_e < 25$ km (approximately) $f(k_t)$ is overestimated, while for $T_e > 25$ km it is underestimated, though the values approach an asymptote of 0.94 which represents a difference of only 6% from the expected value. We conclude, therefore, that $f(k_t)$ is a fair indicator of the actual loading ratio at the coherence transition wavelength, though slight biases do exist, depending upon T_e.

[63] Importantly, the wave number dependence of the recovered f hardly affects recovered T_e estimates, because with the coherence method it is the values of f around the coherence transition wave number that are important in T_e estimation. As *Forsyth* [1985, p. 12,629] notes, "the estimate of elastic thickness from coherence is not very sensitive to uncertainty in f."

10. Results With the Bouguer Admittance

[64] Many authors have chosen to estimate T_e through an admittance analysis. Prior to the arrival of the Bouguer coherence method [*Forsyth*, 1985], this was usually performed by fitting a 1-D theoretically determined admittance curve to the 1-D observed Bouguer admittance, assuming only surface loading [e.g., *McKenzie and Bowin*, 1976; *Banks et al.*, 1977], though *McKenzie and Fairhead* [1997] also used this method with multitaper estimation of the observed free-air admittance. More recently, *Pérez-Gussinyé et al.* [2004] and *Pérez-*

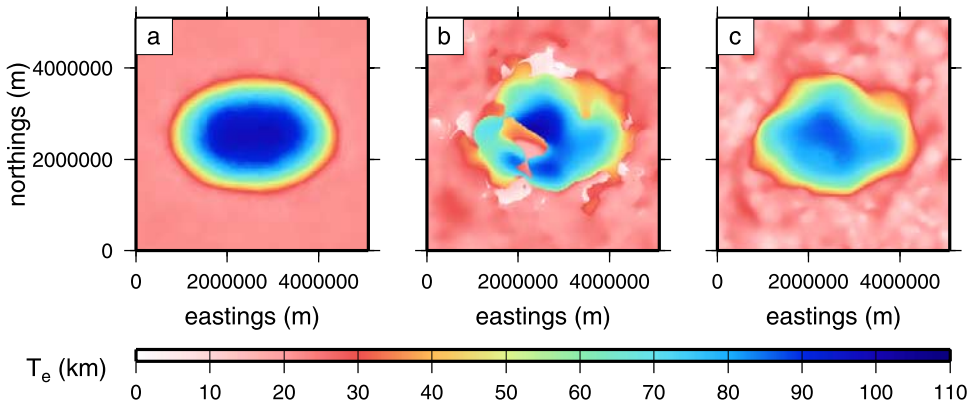

Figure 16. T_e recovery for the high-T_e ellipse (Figure 5a). (a) Average of 100 models from the inversion of the wavelet admittance (mixed loading). (b and c) T_e recovered from model 058 using the admittance and coherence, respectively.

Gussinyé and Watts [2005] computed the elastic thickness of Europe using both Bouguer coherence and free-air admittance with the multitaper method, though instead of fitting the observed data to theoretical expressions, they determined a predicted admittance, as in Forsyth's method, with both surface and subsurface loads.

[65] Here we test the fan wavelet method on (mixed loading) gravity/topography data from the high-T_e elliptical model (Figure 5a), though now fit the Bouguer wavelet admittance. Figure 16a shows the recovered T_e from the average of 100 admittance T_e estimates for this model, and should be compared with Figure 5f which is the result from the Bouguer coherence method. Comparison of the images reveals that, on average, the admittance method recovers the T_e magnitude, and possibly gradient, better than the coherence method. The overall misfit between the elliptical T_e model and recovered average admittance T_e is -0.4 ± 7.7 km (compare 3.0 ± 10.2 km for the coherence method).

[66] However, when individual T_e solutions are considered, rather than an average, the admittance inversion generally gives worse results than when T_e is estimated using the coherence. The admittance T_e results contain more noise than the coherence results, which is most often manifested as abrupt discontinuities in T_e. Figure 16b shows the recovered elliptical T_e for model 058 when the admittance is inverted, while Figure 16c shows the equivalent result for the coherence. It can be seen that the coherence results are generally much smoother than the admittance results which frequently contain spurious T_e anomalies. We also observed that the admittance T_e contains extensive regions where the recovered value is much greater than the input model.

[67] Why should the admittance inversion (1) provide less biased average T_e estimates and (2) be so much more noisy than the coherence inversion? Concerning question 1, we believe this is most likely due to the transition wavelength for the admittance being shorter than that for the coherence (for $f = 1$), so the downward bias in the admittance T_e due to a limited data area size is less pronounced. From *Banks et al.* [2001, Figures 4 and 5] the transition wavelength for $T_e = 90$ km is approximately 630 km for the admittance, and 890 km for the coherence.

[68] Addressing question 2, it is helpful to consider *Forsyth*'s [1985] coherence method. Here, predicted surface and subsurface loads are computed from the observed gravity/topography data assuming a starting value for T_e, and a predicted coherence is then computed from these predicted loads. The T_e value is then adjusted iteratively until the predicted coherence best fits the observed coherence. As *Forsyth* [1985, p. 12,629] notes, solving the loading equations automatically fits the admittance. *Swain and Kirby* [2006] give an example from part of a model where T_e is uniform, which shows an excellent fit between observed and predicted admittance, despite only the coherence being explicitly fitted. However, the loading equations assume uniform T_e, so if T_e varies spatially then only an approximate fit may be expected. In parts of Figure 16c where T_e varies the admittance fit is not so good, but we have noted a tendency for it to be best near the coherence transition wave number (k_t).

[69] When T_e is estimated from the admittance, however, the whole admittance over all wave numbers is explicitly fitted to the predicted admittance, and as noted by *Forsyth* [1985], the admit-

tance is highly sensitive even to slight variations in f, whereas the coherence is not. Therefore, small adjustments of $f(k_t)$ during the coherence inversion do not appreciably alter the estimated T_e. During admittance inversion, on the other hand, it is not just $f(k_t)$ that is important but f at all wave numbers, and the admittance's sensitivity to f means that many different combinations of T_e and $f(k)$ can give predicted admittances that match the observed admittance equally well.

[70] Figure 17 shows slices through the observed and predicted coherence/admittance for the models in Figure 16, together with the loading ratio obtained from the two inversions. (Following the discussion in section 9, we note that the k dependence of f may be artificial, but that $f(k_t)$ is most likely accurate.) In the synthetic models, recall, the random correlations between initial loads alters their effective loading ratio even though they are assigned a specific value within the finite difference routine. For the coherence inversion (Figure 17, left), all slices are relatively smooth. The same cannot be said for the admittance inversions (Figure 17, right), which exhibit many discontinuities. While the observed admittance is reasonably smooth, the inversion has evidently switched between different combinations of T_e and $f(k)$ that, while fitting the local observed admittance well, result in highly variable T_e and f profiles. Whether these poor admittance results apply to real data too remains to be seen, but we suspect that it is so.

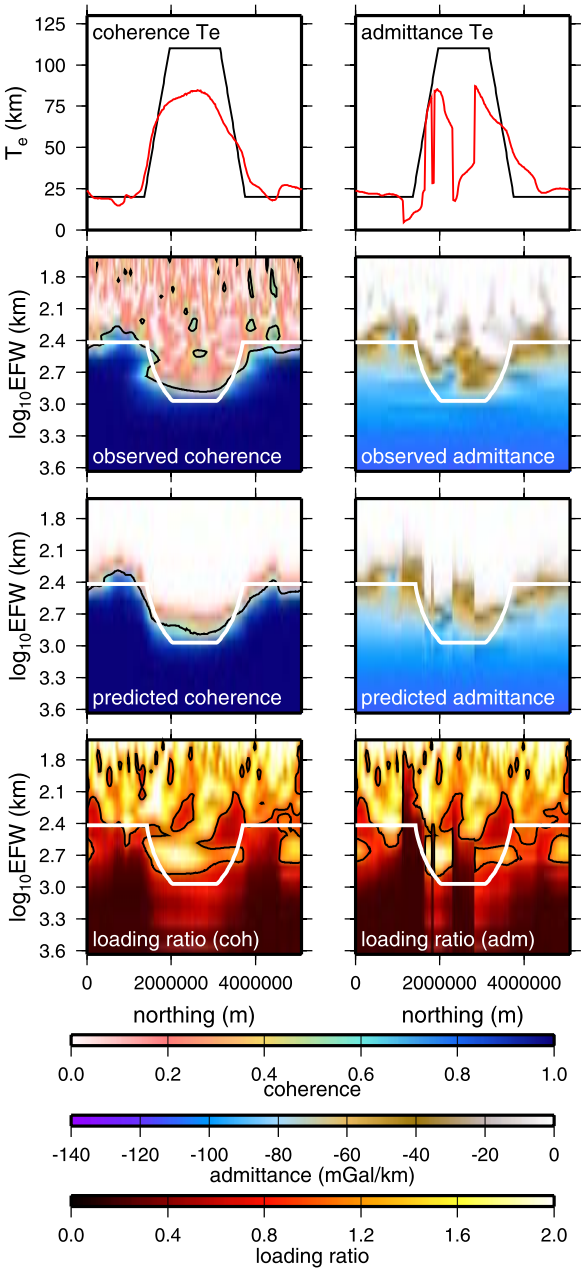

Figure 17. Comparison of the admittance and coherence (observed and predicted) and the loading ratio (from coherence and admittance inversions) for model 058 (mixed loading) of the high-T_e ellipse (Figure 5a). All profiles are extracted at 2000 km easting. The first row shows profiles extracted from the coherence-recovered T_e in Figure 16c, the admittance-recovered T_e in Figure 16b (both red), and from the model T_e in Figure 5a (black). The second row shows the observed coherence and admittance, the third row shows their predicted values, and the fourth row shows the loading ratio recovered from the coherence and admittance inversions. Half-coherence contour is plotted in black in the left-hand plots, the white lines mark the location of the coherence transition wavelengths for the model T_e from equation (D5) for $f = 1$, and EFW is equivalent Fourier wavelength.

11. Conclusions

[71] From our studies on the fan wavelet method and its application to synthetic data, we conclude the following.

[72] 1. We have shown that the land-only load-deconvolution equations may be applied to data over both land and sea, provided the bathymetry is converted to an equivalent topography. For typical values of the Earth's oceanic T_e (15 km), the T_e error committed should be ~3 km, with no error over land.

[73] 2. The synthetic modeling approach will inherently yield T_e underestimates due to the nonzero coherence at all wavelengths between initial random fractal loads which pushes the transition wavelength to smaller values. This phenomenon

will affect all spectral T_e estimation methods, not just the wavelet approach. It will also affect T_e estimation from real data should there exist correlation between initial loads [e.g., *Bechtel et al.*, 1987], though we do not wish to speculate here on the likelihood of such occurrences.

[74] 3. The widths of the transition wavelets impose a fundamental limitation on the resolution of the method. It leads to (1) underestimates of the true T_e when the study area is too small to accommodate the transition wavelets, (2) underestimates of relative T_e differences when the T_e anomaly is narrow compared to its flexural wavelength, and (3) underestimates of steep T_e gradients. Only item 1 is under user control: it requires a judicious choice of study area size (as large as possible) versus grid size (as small as possible), in order to place the transition wavelength in middling values of wavelet scale, where the spatial/spectral resolution is optimal.

[75] 4. Although the resolution of the transition wavelets is probably the most important limitation of the method, there are two other factors that may adversely affect results in the presence of steep T_e gradients. These are (1) the decoupling assumption and (2) the assumption of uniform T_e in the loading equations. We have shown that the decoupling assumption is the most important of these, and that its validity is related to transition wavelet width.

[76] 5. T_e recovery with the wavelet coherence method is only weakly dependent on the fractal dimensions of the synthetic surface and subsurface loads, and their loading ratio.

[77] 6. Inversion of the wavelet admittance leads to large discontinuities in the recovered T_e and f, at least for synthetic data. This is most likely because the admittance is more sensitive to f than is the coherence, and hence we believe it also applies to real data.

[78] 7. Mirroring the gravity/topography data does not affect the T_e recovery ability of the wavelet method as much as it does with Fourier methods. Indeed, this preprocessing technique should be used if a high-T_e structure abuts the data area edge, and/or where the study area is not much larger than the expected transition wavelengths.

Appendix A: Plate Flexure Equation

[79] Consider a thin elastic plate of density ρ_c, which overlies an inviscid fluid of density ρ_m, and is overlain by a fluid of density ρ_f, which may be water ($\rho_f = \rho_w$) or air ($\rho_f = 0$). Following *Forsyth* [1985], the plate is subjected to initial loads of geometrical amplitude h_i at the surface, and w_i at the Moho. In the synthetic modeling procedure, these loads are represented by two random fractal surfaces of equal variance. The Moho load $[(\rho_m - \rho_c)\, g\, w_i]$ is scaled as f times the surface load $[(\rho_c - \rho_f)\, g\, h_i]$, where f is the subsurface-to-surface loading ratio which here we assume to be constant, and g is the acceleration due to gravity (Table 1). For constant $f = f_0$, this essentially gives a random loading ratio with expectation $E[f(k)] = f_0$ at all wave numbers (k) if the fractal dimensions of the two surfaces are equal. If they are not equal, then f will vary with wave number as $f_0 k^{\beta_T - \beta_B}$, where β_T and β_B are the spectral exponents of the surface and subsurface loads, respectively, which are related to fractal dimension (FD) by $\beta = 8 - 2\mathrm{FD}$.

[80] The initial surface load causes a deflection of amplitude w_T at the Moho, resulting in a new surface topography of h_T. The initial load at the Moho causes a deflection of amplitude h_B at the surface, resulting in a new Moho topography of w_B. Here we use the sign convention used by *Forsyth* [1985], though not by *Stark et al.* [2003], that all deflections away from the center of the Earth are positive, whether they occur at the surface or at the Moho. Therefore, the final surface topography after flexure is:

$$h = h_T + h_B \tag{A1}$$

and the final Moho topography after flexure is:

$$w = w_T + w_B \tag{A2}$$

[81] Also, the final deflection amplitude of the plate, v, is the sum of the deflection at the Moho due to the surface load, and the deflection at the surface due to the Moho load:

$$v = w_T + h_B = h - h_i = w - w_i \tag{A3}$$

[82] *Timoshenko and Woinowsky-Krieger* [1959] give the partial differential equation for flexure of an orthotropic plate, i.e., one with orthogonal rigidities $D_x(\mathbf{x})$ and $D_y(\mathbf{x})$, as:

$$-\left(\frac{\partial^2 M_x}{\partial x^2} - 2\frac{\partial^2 M_{xy}}{\partial x\, \partial y} + \frac{\partial^2 M_y}{\partial y^2}\right) + \left(\rho_m - \rho_f\right) g\, v = -\left(\rho_c - \rho_f\right) g\, h_i - \left(\rho_m - \rho_c\right) g\, w_i \tag{A4}$$

[83] Equation (A4) is valid for the deflection of a plate of any rheology [*Burov and Diament*, 1995].

For a thin elastic plate, however, the two bending moments are:

$$M_x = -\left(D_x \frac{\partial^2 v}{\partial x^2} + \nu D_{xy} \frac{\partial^2 v}{\partial y^2}\right) \quad \text{(A5)}$$

$$M_y = -\left(D_y \frac{\partial^2 v}{\partial y^2} + \nu D_{xy} \frac{\partial^2 v}{\partial x^2}\right) \quad \text{(A6)}$$

and the twisting moment is:

$$M_{xy} = (1-\nu) D_{xy} \frac{\partial^2 v}{\partial x \partial y} \quad \text{(A7)}$$

with

$$D_{xy} = \sqrt{D_x D_y} \quad \text{(A8)}$$

and where ν is Poisson's ratio (Table 1). For an isotropic plate, $D_x = D_y = D_{xy} = D$.

[84] For spatially variable rigidities, the final deflections, v, must be solved for by a numerical method. Here we give the finite difference equations for the solution of equation (A4) as coefficients of the indicated $v_{i,j}$ terms, where the i and j subscripts correspond to the x and y directions, respectively, and Δ is the grid spacing in both coordinates:

$$\begin{aligned}
v_{i,j} &: 4\left(D^x_{i,j} + D^y_{i,j} + 2\nu D^{xy}_{i,j}\right) \\
&\quad + \left(D^x_{i+1,j} + D^x_{i-1,j} + D^y_{i,j+1} + D^y_{i,j-1}\right) \\
&\quad + 2(1-\nu)\left(D^{xy}_{i+1,j} + D^{xy}_{i-1,j} + D^{xy}_{i,j+1} + D^{xy}_{i,j-1}\right) \\
&\quad + \left(\rho_m - \rho_f\right) g \Delta^4 \\
v_{i+1,j} &: -2\left(D^x_{i,j} + \nu D^{xy}_{i,j}\right) - 2\left(D^x_{i+1,j} + D^{xy}_{i+1,j}\right) \\
&\quad - (1-\nu)\left(D^{xy}_{i,j+1} + D^{xy}_{i,j-1}\right) \\
v_{i-1,j} &: -2\left(D^x_{i,j} + \nu D^{xy}_{i,j}\right) - 2\left(D^x_{i-1,j} + D^{xy}_{i-1,j}\right) \\
&\quad - (1-\nu)\left(D^{xy}_{i,j+1} + D^{xy}_{i,j-1}\right) \\
v_{i,j+1} &: -2\left(D^y_{i,j} + \nu D^{xy}_{i,j}\right) - 2\left(D^y_{i,j+1} + D^{xy}_{i,j+1}\right) \\
&\quad - (1-\nu)\left(D^{xy}_{i+1,j} + D^{xy}_{i-1,j}\right) \\
v_{i,j-1} &: -2\left(D^y_{i,j} + \nu D^{xy}_{i,j}\right) - 2\left(D^y_{i,j-1} + D^{xy}_{i,j-1}\right) \\
&\quad - (1-\nu)\left(D^{xy}_{i+1,j} + D^{xy}_{i-1,j}\right) \\
v_{i+1,j+1} &: D^{xy}_{i+1,j} + D^{xy}_{i,j+1} + A \\
v_{i+1,j-1} &: D^{xy}_{i+1,j} + D^{xy}_{i,j-1} - A \\
v_{i-1,j+1} &: D^{xy}_{i-1,j} + D^{xy}_{i,j+1} - A \\
v_{i-1,j-1} &: D^{xy}_{i-1,j} + D^{xy}_{i,j-1} + A \\
v_{i+2,j} &: D^x_{i+1,j} \\
v_{i-2,j} &: D^x_{i-1,j} \\
v_{i,j+2} &: D^y_{i,j+1} \\
v_{i,j-2} &: D^y_{i,j-1}
\end{aligned} \quad \text{(A9)}$$

where

$$A = \frac{1-\nu}{8}\left(D^{xy}_{i+1,j+1} - D^{xy}_{i-1,j+1} - D^{xy}_{i+1,j-1} + D^{xy}_{i-1,j-1}\right) \quad \text{(A10)}$$

All the coefficients must be divided by Δ^4.

[85] The final topography and Moho deflection of the synthetic model are then found from equation (A3). The corresponding Bouguer anomaly is obtained from w via the iterative formula of *Parker* [1972].

Appendix B: Fan Wavelet Transform Method

[86] A detailed discussion of the "fan" wavelet method of coherence estimation (both isotropic and anisotropic) is provided by *Kirby and Swain* [2004], *Kirby* [2005] and *Kirby and Swain* [2006]. Furthermore, since other texts discuss the 2-D continuous wavelet transform (CWT) in great depth [e.g., *Farge*, 1992; *Addison*, 2002; *Antoine et al.*, 2004], only those features of the CWT more relevant to the present contribution will be presented here.

B1. Morlet Wavelet

[87] The space domain formula for the 2-D Morlet wavelet at a certain scale, s, is (ignoring azimuthal dependence):

$$\psi_s(\mathbf{x}) = \frac{1}{s} e^{i\mathbf{k}_0 \cdot \mathbf{x}/s} e^{-|\mathbf{x}/s|^2/2} \quad \text{(B1)}$$

[e.g., *Kirby*, 2005], where the "central wave number" of the Morlet wavelet is:

$$|\mathbf{k}_0| = \pi \sqrt{\frac{2}{\ln 2}} \quad \text{(B2)}$$

[e.g., *Addison*, 2002]. In order to enable a direct comparison between Fourier spectra and the wavelet coefficients at a particular scale, each scale is interpreted as an equivalent Fourier wave number (κ), which for the Morlet wavelet is given by:

$$\kappa = \frac{|\mathbf{k}_0|}{s} \quad \text{(B3)}$$

or, in terms of an equivalent Fourier wavelength:

$$\lambda_e = \frac{2\pi s}{|\mathbf{k}_0|} \quad \text{(B4)}$$

since $\kappa = 2\pi/\lambda_e$. It can be shown that the width of the Gaussian envelope of this wavelet, at a fraction p of the maximum value ($0 < p < 1$), is:

$$\Delta_\psi(\lambda_e, p) = \frac{\lambda_e |\mathbf{k}_0|}{\pi} \sqrt{-2 \ln p} \tag{B5}$$

using equation (B4).

[88] Finally, to support the observation by *Kirby* [2005] that the Morlet wavelet gives a wavelet power spectrum that very closely reproduces the radially averaged Fourier power spectrum, we calculate the Morlet wavelet transform of a 2-D complex exponential of a single wave number, $|\mathbf{k}_1|$. For $g(\mathbf{x}) = e^{i\mathbf{k}_1 \cdot \mathbf{x}}$, its Morlet wavelet transform is:

$$\tilde{g}(s, \mathbf{x}) = e^{i\mathbf{k}_1 \cdot \mathbf{x}} e^{-|s\mathbf{k}_1 - \mathbf{k}_0|^2/2} \tag{B6}$$

which is just the input signal, though amplitude-normalized by a factor dependent on the difference between the input wave number and the central wave number of the Morlet wavelet. Hence, Morlet wavelets can be used to generate coherences and admittances that may be directly compared with the Fourier-derived predictions of theory, without the need for further numerical integrations that must be performed with other wavelets [*Kirby and Swain*, 2004].

B2. Wavelet Coherence and Admittance

[89] Computing the wavelet coefficients by means of the space domain convolution of equation (2) is time consuming, so it is generally carried out by multiplication in the wave number domain via the Fourier transform ($\mathbf{F}$), e.g., $\tilde{b}(\kappa, \mathbf{x}, \theta) = \mathbf{F}^{-1}\{\hat{b}\hat{\psi}_{s\theta}\}$ for the Bouguer anomaly, where a $\hat{}$ indicates a Fourier transform. Note that with the relationship between scale and equivalent Fourier wave number, equation (B3), we now write κ instead of s in the wavelet coefficients. We use the mixed radix fast Fourier transform (FFT) algorithm of *Singleton* [1968], which requires only that the array dimensions be products of prime numbers ($\leq$67), rather than a power of two [see also *Kirby*, 2002].

[90] Whereas the traditional periodogram method of coherence estimation [e.g., *Forsyth*, 1985; *Zuber et al.*, 1989] performs averaging of the Fourier autospectra and cross-spectra between gravity and topography over isotropic annuli in the wave number domain, the fan wavelet method averages the wavelet autospectra and cross-spectra in the wavelet domain over separate azimuths, θ, where $0° < \theta < 180°$:

$$E_{pq}(\kappa, \mathbf{x}) = \frac{1}{N_\theta} \sum_\theta \{\tilde{p}\, \tilde{q}^*\} \tag{B7}$$

for any $\tilde{p}(\kappa, \mathbf{x}, \theta)$, $\tilde{q}(\kappa, \mathbf{x}, \theta)$. The observed wavelet coherence can now be computed through:

$$\gamma^2_w(\kappa, \mathbf{x}) = \frac{E_{bh}(\kappa, \mathbf{x})\, E^*_{bh}(\kappa, \mathbf{x})}{E_{bb}(\kappa, \mathbf{x})\, E_{hh}(\kappa, \mathbf{x})} \tag{B8}$$

This quantity contains, at each grid node, an estimate of the observed coherence between the Bouguer anomaly and equivalent topography.

[91] If desired, the wavelet admittance is obtained from:

$$Q_w(\kappa, \mathbf{x}) = \frac{\Re[E_{bh}(\kappa, \mathbf{x})]}{E_{hh}(\kappa, \mathbf{x})} \tag{B9}$$

This is computed using the real part of the $\tilde{b}\tilde{h}^*$ cross-spectrum, which is more in keeping with the conventional definition of the classical Fourier (1-D) admittance in which the isotropic annular averaging effectively removes its imaginary part.

Appendix C: Inversion Methods

[92] To invert the observed wavelet coherence (or admittance), at each grid node, in order to obtain estimates of effective elastic thickness, T_e, and subsurface-to-surface loading ratio, f, we use wavelet transform adaptations of the thin elastic plate models of *Forsyth* [1985] and *Banks et al.* [2001]. Owing to the relationship between Morlet wavelet spectra and Fourier spectra, equation (B6), the wavelet versions of their equations are identical to the Fourier equations, but with Fourier transforms replaced by Morlet wavelet transforms, and wave number replaced by equivalent Fourier wave number, equation (B3). Here we give the full mixed-loading equations for completeness, with ρ_f being the density of the overlying fluid (air or water). When used with equivalent topography, the inversion methods require $\rho_f = 0$ (though see Appendix C3).

[93] As discussed in section 3.4, the inversion makes two assumptions; those of spatial decoupling of local wavelet spectra, and of uniform T_e (see also sections 6 and 8). T_e at a grid node is then found by minimizing the predicted against the observed wavelet coherence (or admittance), using Brent's method of 1-D minimization [*Press et al.*,

1992], with the observed – predicted differences weighted by the inverse of equivalent Fourier wave number [*Kirby and Swain*, 2006].

C1. Forsyth Method

[94] Wavelet transforms of the initial Moho and surface load topographies ($\tilde{w}_i$ and $\tilde{h}_i$), are found from the observed Moho and surface topographies ($\tilde{w}$ and $\tilde{h}$) via the so-called "load-deconvolution equations":

$$\begin{pmatrix} \tilde{h} \\ \tilde{w} \end{pmatrix} = \frac{1}{\xi + r} \begin{pmatrix} \xi & -1 \\ -r & r\phi \end{pmatrix} \begin{pmatrix} \tilde{h}_i \\ \tilde{w}_i \end{pmatrix} \tag{C1}$$

[cf. *Forsyth*, 1985] where the subsurface loading occurs at the Moho, and where the density ratio, r, is:

$$r \equiv \frac{\rho_c - \rho_f}{\rho_m - \rho_c} \tag{C2}$$

The parameters ξ and ϕ are:

$$\xi(\kappa) = 1 + \frac{D\kappa^4}{(\rho_m - \rho_c)\, g} \tag{C3}$$

$$\phi(\kappa) = 1 + \frac{D\kappa^4}{\left(\rho_c - \rho_f\right) g} \tag{C4}$$

where κ is the equivalent Fourier wave number. The flexural rigidity, D, is related to the elastic thickness by:

$$D = \frac{E\, T_e^3}{12(1 - \nu^2)} \tag{C5}$$

The symbols and values of the constants are given in Table 1.

[95] The wavelet transform of the Moho topography ($\tilde{w}$) is derived by downward continuation of the wavelet transform of the observed Bouguer anomaly:

$$\tilde{w}(\kappa, \mathbf{x}, \theta) = \frac{e^{\kappa z_m(\mathbf{x})}}{2\pi G(\rho_m - \rho_c)}\, \tilde{b} \tag{C6}$$

which is the first term of the *Parker* [1972] series, and where G is the Newtonian gravitational constant (Table 1). Note that the depth to the Moho, z_m, and even the densities are allowed to vary over geographic location, because the inversions are performed at each grid cell independently, subject to the decoupling assumption.

[96] The surface ($_T$) and subsurface ($_B$) components of the Moho and surface topography after loading are obtained from equations (C1) and (A1), (A2), and (A3). Then, the predicted wavelet coherence is:

$$\gamma^2_{w,p}(\kappa, \mathbf{x}) = \frac{\left(E^T_{wh} + E^B_{wh}\right)\left(E^T_{wh} + E^B_{wh}\right)^*}{\left(E^T_{ww} + E^B_{ww}\right)\left(E^T_{hh} + E^B_{hh}\right)} \tag{C7}$$

where azimuthal averaging of the various auto-spectra and cross-spectra is represented by:

$$E^{\sigma}_{pq}(\kappa, \mathbf{x}) = \frac{1}{N_\theta} \sum_\theta \{\tilde{p}_\sigma\, \tilde{q}^*_\sigma\} \tag{C8}$$

where $\tilde{p}$, $\tilde{q}$ are either $\tilde{w}$ or $\tilde{h}$; and σ is either T for surface load components, or B for subsurface load components.

[97] A predicted wavelet admittance may also be computed:

$$Q_{w,p}(\kappa, \mathbf{x}) = -2\pi G\left(\rho_c - \rho_f\right) e^{-\kappa z_m} \frac{E'_{hh}}{E^T_{hh} + E^B_{hh}} \tag{C9}$$

where:

$$E'_{hh}(\kappa, \mathbf{x}) = \frac{1}{N_\theta} \sum_\theta \left\{ \frac{|\tilde{h}_T|^2}{\xi} + \phi |\tilde{h}_B|^2 \right\} \tag{C10}$$

[98] If desired, a wavelet loading ratio can be derived from the initial loads:

$$f_W(\kappa, \mathbf{x}) = \frac{1}{r} \sqrt{\frac{E^i_{ww}}{E^i_{hh}}} \tag{C11}$$

using $\sigma = i$ in equation (C8). To display maps of the loading ratio, we average $f_W(\kappa, \mathbf{x})$ at three of its values around the transition wave number, where the predicted wavelet coherence has a value of $\frac{1}{2}$.

C2. Banks Method

[99] In the *Banks et al.* [2001] formulation of the thin plate model, the internal loading occurs at a thin layer at depth z_l ($<z_m$) within the crust. Importantly, the actual magnitude of the thin layer's density does not need to be known. As for the Forsyth approach with a variable $z_m(\mathbf{x})$, the wavelet-adapted equations for the Banks method can account for a variable $z_l(\mathbf{x})$ if this information is known. Generally speaking, the inclusion of a thin layer between the surface and Moho serves to reduce T_e estimates, though not significantly, with *Lowry and Smith* [1994], *Wang and Mareschal*

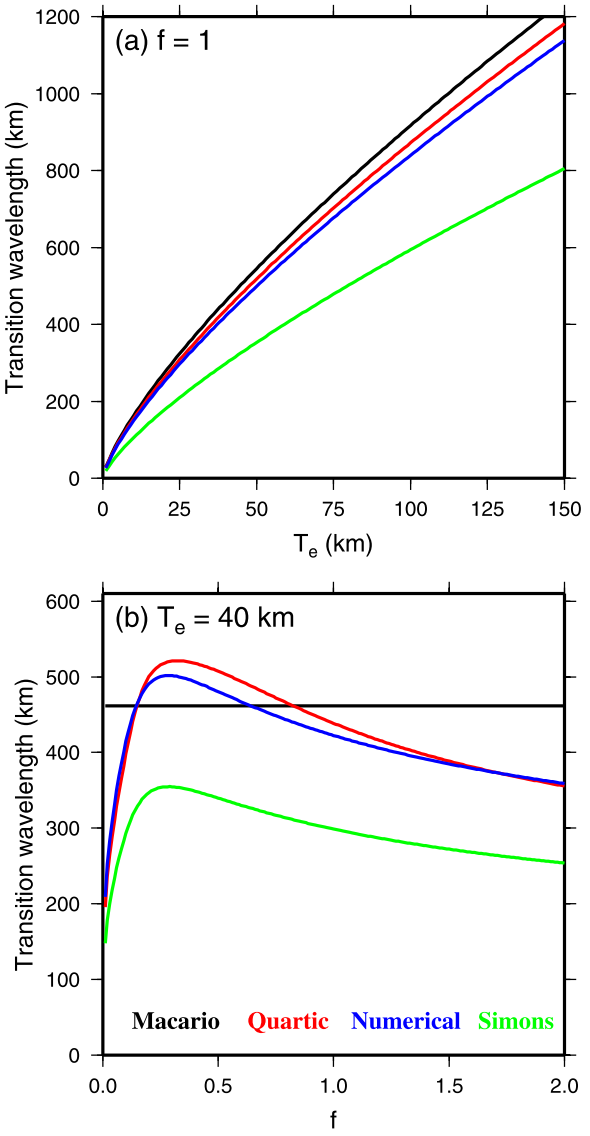

Figure C1. The coherence transition wavelength from three methods, for $\rho_f = 0$. (a) Its variation as a function of T_e for $f = 1$ and (b) its variation as a function of f for T_e = 40 km. Red curves show the solutions from the quartic equation, green curves are from *Simons and van der Hilst* [2003], and blue curves are from numerical interpolation of the theoretical coherence formula. The black curve shows the flexural wavelength given by *Macario et al.* [1995], which is f-independent.

[1999] and *Flück et al.* [2003] finding their results to be fairly insensitive to the magnitude of the density contrasts or depth of the interface, albeit using different approaches to that of *Banks et al.* [2001].

[100] Wavelet transforms of the initial surface and internal loads ($\tilde{\ell}_T$ and $\tilde{\ell}_B$), are found from the observed Bouguer anomaly and equivalent topography wavelet transforms ($\tilde{b}$ and $\tilde{h}$) via the load-deconvolution equations:

$$\begin{pmatrix} \tilde{b} \\ \tilde{h} \end{pmatrix} = \begin{pmatrix} \alpha_T & \alpha_B \\ \beta_T & \beta_B \end{pmatrix} \begin{pmatrix} \tilde{\ell}_T \\ \tilde{\ell}_B \end{pmatrix} \tag{C12}$$

where the parameters are:

$$\begin{aligned} \alpha_T(\kappa) &= \frac{-2\pi G(\rho_m - \rho_c)e^{-\kappa z_m}}{D\kappa^4 + \left(\rho_m - \rho_f\right)g} \\ \alpha_B(\kappa) &= \alpha_T + \frac{2\pi G\, e^{-\kappa z_l}}{g} \\ \beta_T(\kappa) &= \beta_B + \frac{1}{\left(\rho_c - \rho_f\right)g} \\ \beta_B(\kappa) &= \frac{-1}{D\kappa^4 + \left(\rho_m - \rho_f\right)g} \end{aligned} \tag{C13}$$

(see Table 1 for symbols and values of the constants). The components of the Bouguer anomaly and equivalent topography due to surface and subsurface loads are: $\tilde{b}_T = \alpha_T \tilde{\ell}_T$, $\tilde{b}_B = \alpha_B \tilde{\ell}_B$, $\tilde{h}_T = \beta_T \tilde{\ell}_T$, and $\tilde{h}_B = \beta_B \tilde{\ell}_B$, enabling the estimation of the predicted wavelet coherence:

$$\gamma^2_{W,p}(\kappa, \mathbf{x}) = \frac{\left(E^T_{bh} + E^B_{bh}\right)\left(E^T_{bh} + E^B_{bh}\right)^*}{\left(E^T_{bb} + E^B_{bb}\right)\left(E^T_{hh} + E^B_{hh}\right)} \tag{C14}$$

where the E^{σ}_{pq} are given by equation (C8).

[101] The predicted wavelet admittance may also be computed, through:

$$Q_{W,p}(\kappa, \mathbf{x}) = \frac{E'_{hh}}{E^T_{hh} + E^B_{hh}} \tag{C15}$$

where

$$E'_{hh}(\kappa, \mathbf{x}) = \frac{1}{N_\theta} \sum_\theta \left\{ \frac{\alpha_T}{\beta_T} |\tilde{h}_T|^2 + \frac{\alpha_B}{\beta_B} |\tilde{h}_B|^2 \right\} \tag{C16}$$

[102] The wavelet loading ratio is then:

$$f_W(\kappa, \mathbf{x}) = \sqrt{\frac{E^B_{\ell\ell}}{E^T_{\ell\ell}}} \tag{C17}$$

where the $E^{\sigma}_{\ell\ell}$ are given by equation (C8) for $p = q = \ell$.

C3. Equivalent Topography Approximation

[103] As discussed in section 2.2, in oceanic regions we convert actual topography (h) to an equivalent topography [$h' = (\rho_c - \rho_w)h/\rho_c$], and propose that this enables the use of the land-loading thin elastic plate equations. Now, in equation (C1) as we compute it, the h is actually h', and

it can be shown that $rh' = rh$ when $\rho_f = 0$. That is, to a first approximation, using $\rho_f = 0$ and h' is equivalent to using $\rho_f = \rho_w$ and h at sea. However, this substitution does not alter the expression for ϕ for example (equation (C4)), when it ought to, meaning that at sea, we are using a "land ϕ" when we should be using a "sea ϕ."

[104] The effect of this on T_e can be determined through our new solution to the quartic equation describing half-coherence, which provides an analytic expression relating T_e, f and the coherence transition wave number k_t (Appendix D). It can be shown that, when $\rho_f = 0$ in equation (D3), T_e is systematically larger than when $\rho_f = \rho_w$, for all values of transition wavelength (λ_t); though the reverse is true when $f < 0.3$. This means that our use of $\rho_f = 0$ in the deconvolution equations is biasing T_e, but in oceanic areas only. However, T_e generally does not exceed 40 km over the Earth's oceans [*Watts*, 2001]. So, using our quartic solutions we find pairs of allowable values of f and λ_t that give $T_e = 40$ km with $\rho_f = \rho_w$: these pairs follow a locus similar to the red curve in Figure C1b. Then, for each pair we calculate T_e with $\rho_f = 0$, and subtract 40 km from this value. In this manner, we find that oceanic T_e will be underestimated by a maximum of 4 km when $f < 0.3$, and overestimated by a maximum of 7 km when $f > 0.3$. For a more realistic value of mean oceanic T_e, say 15 km, these limits are −1 and +3 km.

[105] The effect on f is the reverse: using $\rho_f = 0$ in the deconvolution equations biases f to smaller values in oceanic areas, by up to 1 unit when $f \sim 5$.

Appendix D: Coherence Transition Wavelength

[106] The predicted coherence formula of *Forsyth* [1985] can be expressed in analytic form as:

$$\gamma^2(k) = \frac{(\xi + \phi f^2 r^2)^2}{(\xi^2 + f^2 r^2)(1 + \phi^2 f^2 r^2)} \tag{D1}$$

where f is the initial subsurface-to-surface loading ratio, r is the density ratio given by:

$$r \equiv \frac{\Delta\rho_1}{\Delta\rho_2} \tag{D2}$$

(see equation (C2)) with

$$\Delta\rho_1 = \rho_c - \rho_f \quad \Delta\rho_2 = \rho_m - \rho_c \tag{D3}$$

and where

$$\xi(k) = 1 + \frac{Dk^4}{g\Delta\rho_2} \quad \phi(k) = 1 + \frac{Dk^4}{g\Delta\rho_1} \tag{D4}$$

(see equations (C3) and (C4)) where k is 1-D wave number, D is flexural rigidity, and the other constants are listed in Table 1. We set the density of the overlying fluid, ρ_f, to zero, though see the discussion in Appendix C3.

[107] The transition from supported to compensated loads is defined to occur at a "transition wave number," k_t, such that $\gamma^2(k_t) = \frac{1}{2}$. Under this criterion, equation (D1) becomes a quartic equation in k_t^4:

$$\chi^4 + a\chi^3 + b\chi^2 + c\chi + d = 0 \tag{D5}$$

where

$$\chi = \frac{Dk_t^4}{g} \tag{D6}$$

and where the coefficients can be shown to be:

$$\begin{aligned} a &= 2(\Delta\rho_1 + \Delta\rho_2) \\ b &= -\left(\frac{1 - f^2r^2}{f^2r^2}\right)(\Delta\rho_1^2 - \Delta\rho_2^2 f^2 r^2) \\ c &= -2\left(\frac{1 + f^2r^2}{f^2r^2}\right)\Delta\rho_1\Delta\rho_2(\Delta\rho_1 + \Delta\rho_2 f^2 r^2) \\ d &= -\left(\frac{1 + f^2r^2}{f^2r^2}\right)\Delta\rho_1^2\Delta\rho_2^2 \end{aligned} \tag{D7}$$

We solved equation (D5) using Ferrari's method [e.g., *Korn and Korn*, 1961], given by *Claessens* [2000] as:

$$\begin{aligned} p &= -\frac{b^2}{3} + \frac{ac}{4} - d \\ q &= -\frac{2b^3}{27} + \frac{b(ac - 4d)}{12} + \frac{2bd - c^2 - a^2 d}{8} \\ R &= \frac{p^3}{27} + \frac{q^2}{4} \\ t &= \sqrt[3]{-\frac{q}{2} + \sqrt{R}} + \sqrt[3]{-\frac{q}{2} - \sqrt{R}} \\ S &= \frac{1}{2}\left(\frac{a}{2} - \sqrt{\frac{a^2}{4} + 2t - b}\right) \\ T &= t - \sqrt{t^2 - d} \\ \chi &= -S + \sqrt{S^2 - T} \end{aligned} \tag{D8}$$

Note we present the solution for only one of the four roots of equation (D5), since the other three are complex. The transition wave number may then be found from equation (D6), and the transition

wavelength from $\lambda_t = 2\pi/k_t$. Figure C1a shows the variation of the transition wavelength as a function of T_e (red curve), for constant f.

[108] To check the accuracy of our solution of the quartic equation, we also used *Simons and van der Hilst* [2003, equations (5) and (6)] (green curve in Figure C1a), and also carried out a direct interpolation of numerical values of the theoretical coherence formula (equation (D1)) to find the wavenumber/wavelength corresponding to $\gamma^2(k) = \frac{1}{2}$ (blue curve). Finally, the black curve in Figure C1a shows the flexural wavelength given by *Macario et al.* [1995, equation (2)], which is independent of loading ratio.

[109] As can be seen, the numerical and quartic solutions are fairly similar, which supports our quartic solution. However, both differ markedly from the solution of *Simons and van der Hilst* [2003], which we suspect is in error.

[110] Figure C1b shows the variation of the transition wavelength with loading ratio, for a constant T_e. From numerical testing, we found that the location of the turning point for the quartic solution is at $f \approx 0.32$ for all T_e values, and that the flexural wavelength and the transition wavelength are equal when $f \approx 0.15$ and 0.83, again for all T_e values.

Acknowledgments

[111] We are grateful to Marta Pérez-Gussinyé and Tony Lowry for their very constructive reviews. Most figures were plotted using GMT [*Wessel and Smith*, 1998]. This is TIGeR publication 95.

References

Addison, P. S. (2002), *The Illustrated Wavelet Transform Handbook*, Inst. of Phys. Publ., Bristol, U. K.

Antoine, J.-P., R. Murenzi, P. Vandergheynst, and S. T. Ali (2004), *Two-Dimensional Wavelets and Their Relatives*, Cambridge Univ. Press, Cambridge, U. K.

Banks, R. J., R. L. Parker, and S. P. Huestis (1977), Isostatic compensation on a continental scale: Local versus regional mechanisms, *Geophys. J. R. Astron. Soc.*, *51*, 431–452.

Banks, R. J., S. C. Francis, and R. G. Hipkin (2001), Effects of loads in the upper crust on estimates of the elastic thickness of the lithosphere, *Geophys. J. Int.*, *145*, 291–299.

Bechtel, T. D., D. W. Forsyth, and C. J. Swain (1987), Mechanisms of isostatic compensation in the vicinity of the East African Rift, Kenya, *Geophys. J. R. Astron. Soc.*, *90*, 445–465.

Braitenberg, C., J. Ebbing, and H.-J. Gotze (2002), Inverse modelling of elastic thickness by convolution method—The Eastern Alps as a case example, *Earth Planet. Sci. Lett.*, *202*, 387–404.

Burov, E. B., and M. Diament (1995), The effective elastic thickness (T_e) of continental lithosphere: What does it really mean?, *J. Geophys. Res.*, *100*(B3), 3905–3927.

Claessens, S. J. (2000), Computation of geographical from Cartesian co-ordinates (in Dutch), case study report, Dep. of Geod., Delft Univ. of Technol., Delft, Netherlands.

Daly, E., C. Brown, C. P. Stark, and C. J. Ebinger (2004), Wavelet and multitaper coherence methods for assessing the elastic thickness of the Irish Atlantic margin, *Geophys. J. Int.*, *159*, 445–459.

Farge, M. (1992), Wavelet transforms and their applications to turbulence, *Annu. Rev. Fluid Mech.*, *24*, 395–457.

Flück, P., R. D. Hyndman, and C. Lowe (2003), Effective elastic thickness Te of the lithosphere in western Canada, *J. Geophys. Res.*, *108*(B9), 2430, doi:10.1029/2002JB002201.

Forsyth, D. W. (1985), Subsurface loading and estimates of the flexural rigidity of continental lithosphere, *J. Geophys. Res.*, *90*(B14), 12,623–12,632.

Hartley, R., A. B. Watts, and J. D. Fairhead (1996), Isostasy of Africa, *Earth Planet. Sci. Lett.*, *137*, 1–18.

Kirby, J. F. (2002), A FORTRAN90 subroutine to calculate array sizes prior to a mixed-radix fast Fourier transform, *Comput. Geosci.*, *28*, 999–1001.

Kirby, J. F. (2005), Which wavelet best reproduces the Fourier power spectrum?, *Comput. Geosci.*, *31*(7), 846–864.

Kirby, J. F., and C. J. Swain (2004), Global and local isostatic coherence from the wavelet transform, *Geophys. Res. Lett.*, *31*, L24608, doi:10.1029/2004GL021569.

Kirby, J. F., and C. J. Swain (2006), Mapping the mechanical anisotropy of the lithosphere using a 2D wavelet coherence, and its application to Australia, *Phys. Earth Planet. Inter.*, *158*, 122–138.

Korn, G. A., and T. M. Korn (1961), *Mathematical Handbook for Scientists and Engineers*, McGraw-Hill, New York.

Lowry, A. R., and R. B. Smith (1994), Flexural rigidity of the Basin and Range–Colorado Plateau–Rocky Mountain transition from coherence analysis of gravity and topography, *J. Geophys. Res.*, *99*(B10), 20,123–20,140.

Macario, A., A. Malinverno, and W. F. Haxby (1995), On the robustness of elastic thickness estimates obtained using the coherence method, *J. Geophys. Res.*, *100*(B8), 15,163–15,172.

McKenzie, D. (2003), Estimating T_e in the presence of internal loads, *J. Geophys. Res.*, *108*(B9), 2438, doi:10.1029/2002JB001766.

McKenzie, D. P., and C. Bowin (1976), The relationship between bathymetry and gravity in the Atlantic Ocean, *J. Geophys. Res.*, *81*(11), 1903–1915.

McKenzie, D., and J. D. Fairhead (1997), Estimates of the effective elastic thickness of the continental lithosphere from Bouguer and free air gravity anomalies, *J. Geophys. Res.*, *102*(B12), 27,523–27,552.

Ojeda, G. Y., and D. Whitman (2002), Effect of windowing on lithosphere elastic thickness estimates obtained via the coherence method: Results from northern South America, *J. Geophys. Res.*, *107*(B11), 2275, doi:10.1029/2000JB000114.

Parker, R. L. (1972), The rapid calculation of potential anomalies, *Geophys. J. R. Astron. Soc.*, *31*, 447–455.

Peitgen, H.-O., and D. Saupe (1988), *The Science of Fractal Images*, Springer, New York.

Pérez-Gussinyé, M., and A. B. Watts (2005), The long-term strength of Europe and its implications for plate-forming processes, *Nature*, *436*(7049), 381–384.

Pérez-Gussinyé, M., A. R. Lowry, A. B. Watts, and I. Velicogna (2004), On the recovery of effective elastic thickness using

spectral methods: Examples from synthetic data and from the Fennoscandian Shield, *J. Geophys. Res.*, *109*, B10409, doi:10.1029/2003JB002788.

Poudjom Djomani, Y. H., J. D. Fairhead, and W. L. Griffin (1999), The flexural rigidity of Fennoscandia: Reflection of the tectonothermal age of the lithospheric mantle, *Earth Planet. Sci. Lett.*, *174*, 139–154.

Press, W. H., S. A. Teukolsky, W. T. Vetterling, and B. P. Flannery (1992), *Numerical Recipes in Fortran 77*, 2nd ed., Cambridge Univ. Press, Cambridge, U. K.

Simons, F. J., and R. D. van der Hilst (2003), Seismic and mechanical anisotropy and the past and present deformation of the Australian lithosphere, *Earth Planet. Sci. Lett.*, *211*, 271–286.

Simons, F. J., M. T. Zuber, and J. Korenaga (2000), Isostatic response of the Australian lithosphere: Estimation of effective elastic thickness and anisotropy using multitaper spectral analysis, *J. Geophys. Res.*, *105*(B8), 19,163–19,184.

Singleton, R. C. (1968), An algorithm for computing the mixed radix fast Fourier transform, *IEEE Trans. Audio Electroacoust.*, *AU-17*(2), 93–102.

Stark, C. P., J. Stewart, and C. J. Ebinger (2003), Wavelet transform mapping of effective elastic thickness and plate loading: Validation using synthetic data and application to the study of southern African tectonics, *J. Geophys. Res.*, *108*(B12), 2558, doi:10.1029/2001JB000609.

Stephen, J., S. B. Singh, and D. B. Yedekar (2003), Elastic thickness and isostatic coherence anisotropy in the South Indian Peninsular Shield and its implications, *Geophys. Res. Lett.*, *30*(16), 1853, doi:10.1029/2003GL017686.

Swain, C. J., and J. F. Kirby (2003), The effect of 'noise' on estimates of the elastic thickness of the continental lithosphere by the coherence method, *Geophys. Res. Lett.*, *30*(11), 1574, doi:10.1029/2003GL017070.

Swain, C. J., and J. F. Kirby (2006), An effective elastic thickness map of Australia from wavelet transforms of gravity and topography using Forsyth's method, *Geophys. Res. Lett.*, *33*, L02314, doi:10.1029/2005GL025090.

Tassara, A., C. J. Swain, R. I. Hackney, and J. F. Kirby (2007), Elastic thickness structure of South America estimated using wavelets and satellite-derived gravity data, *Earth Planet. Sci. Lett.*, *253*, 17–36.

Timoshenko, S. P., and S. Woinowsky-Krieger (1959), *Theory of Plates and Shells*, 2nd ed., McGraw-Hill, New York.

Wang, Y., and J.-C. Mareschal (1999), Elastic thickness of the lithosphere in the Central Canadian Shield, *Geophys. Res. Lett.*, *26*(19), 3033–3035.

Watts, A. B. (2001), *Isostasy and Flexure of the Lithosphere*, Cambridge Univ. Press, Cambridge, U. K.

Wessel, P., and W. H. F. Smith (1998), New, improved version of Generic Mapping Tools released, *Eos Trans. AGU*, *79*(47), 579.

Zuber, M. T., T. D. Bechtel, and D. W. Forsyth (1989), Effective elastic thickness of the lithosphere and the mechanisms of isostatic compensation in Australia, *J. Geophys. Res.*, *94*(B7), 9353–9367.